UNIVERSITY OF CALIFORNIA, SAN DIEGO

Synthesis of a New Class of High-Entropy ABO_3 Perovskites

A thesis submitted in partial satisfaction of the
requirements for the degree Master of Science

in

Materials Science and Engineering

by

Sicong Jiang

Committee in charge:

Professor Jian Luo, Chair
Professor Kenneth S. Vecchio
Professor Kesong Yang

2017

The Thesis of Sicong Jiang is approved, and it is acceptable in quality and form for publication on microfilm and electronically:

_____

_____

_____

Chair

University of California, San Diego

2017

DEDICATION

To Guiping Chen, Jianjun Jiang, and Bangbo Ling

TABLE OF CONTENTS

LIST OF FIGURES

LIST OF TABLES

ACKNOWLEDGEMENTS

Firstly, I would like to appreciate my advisor, Dr. Jian Luo, for giving me the chance to finish this research. Dr. Jian Luo is very helpful and always willing to help his students. He is also full of knowledge; every time when I struggled with experiments and results, he gave me some pertinent suggestions which guided me to move on and gave me courage. In the first few months on this research, I knew little about how to do scientific research; however, Dr. Jian Luo taught me how to design experiments, how to prove conjectures, how to present data, and how to be a true scientist. I'm very glad to discuss with him during the regular 1:1 meeting every two weeks, where I learnt a lot of important things to do scientific research. It is Dr. Jian Luo that makes this thesis come true. I also want to thank Dr. Kenneth S. Vecchio for his help on equipment and guidance in research and to thank Dr. Kesong Yang for his help on DFT calculations.

Secondly, I would like to express my deep and sincere gratitude to Joshua Gild who taught me almost everything from scratch patiently. Besides, I would like to thank my other collaborators Naixie Zhou, who also gives me a lot of pertinent suggestions, Dr. Yuanyao Zhang, Jiajia Huang, Dr. Tao Hu, who helped me take STEM images, Dr. Shengfeng Yang, Mingde Qin, who will be a PhD candidate this year, Jiuyuan Nie, who will definitely be a PhD candidate this March as well, Mojitaba Samiee, and other people who helped me during my research.

Finally, I would like to appreciate my parents Guiping Chen and Jianjun Jiang, without whom I would not have the chance to study in the United States of America. I regret that I cannot accompany with them these two years. Moreover, I would like to

express my gratitude to my best friends Bangbo Ling, who gives me the courage and motivation to study in the United States of America.

VITA

2015 B.S. Zhengzhou University, People's Republic of China

2017 M.S. University of California, San Diego, USA

PUBLICATIONS

1. J. Gild, Y. Zhang, T. Harrington, **S. Jiang**, T. Hu, M. C. Quinn, W. M. Miller, N. Zhou, K. Vecchio, J. Luo, "High-Entropy Metal Diborides: A New Class of High-Entropy Materials and a New Type of Ultrahigh Temperature Ceramics," Scientific Reports, 6: 37946 (2016)

ABSTRACT OF THE THESIS

Synthesis of a New Class of High-Entropy ABO_3 Perovskites

by

Sicong Jiang

Master of Science in Materials Science and Engineering

University of California, San Diego, 2017

Professor Jian Luo, Chair

The perovskite structure is very common in ceramics. In this thesis, eleven kinds of high-entropy ABO_3 perovskites, with five equimolar atoms in B sites, were successfully synthesized by high-energy ball milling and conventional pressureless sintering. Six of them, compositions #S1, $Sr(Zr_{0.2}Sn_{0.2}Ti_{0.2}Hf_{0.2}Mn_{0.2})O_3$, #S5, $Sr(Zr_{0.2}Sn_{0.2}Ti_{0.2}Hf_{0.2}Nb_{0.2})O_3$, #B2, $Ba(Zr_{0.2}Sn_{0.2}Ti_{0.2}Hf_{0.2}Ce_{0.2})O_3$, #B3, $Ba(Zr_{0.2}Sn_{0.2}Ti_{0.2}Hf_{0.2}Y_{0.2})O_{3-x}$, #B5, $Ba(Zr_{0.2}Sn_{0.2}Ti_{0.2}Hf_{0.2}Nb_{0.2})O_3$, and #BS1, $(Ba_{0.5}Sr_{0.5})(Zr_{0.2}Sn_{0.2}Ti_{0.2}Hf_{0.2}Nb_{0.2})O_3$, can form a cubic homogeneous single phase, while the others showed a major cubic phase with different amount of secondary phases. Phase purity was verified by energy dispersive x-ray spectroscopy (EDS) mapping.

Quench experiments were carried out to prove that composition #S1, $Sr(Zr_{0.2}Sn_{0.2}Ti_{0.2}Hf_{0.2}Mn_{0.2})O_3$, is an entropy stabilized perovskite, which is also characterized in atomic and nanoscale by aberration-corrected scanning transmission electron microscopy (AC STEM), STEM high-angle annular dark-field (HAADF) images, and STEM annular bright-field (ABF) images. Goldschmidt's tolerance factor (t) was introduced to be a necessary, but not sufficient, condition to form a homogeneous single phase, while the revised Hume-Ruthery rule for high-entropy alloys (HEAs) can not extend to the case of high-entropy ABO_3 perovskites. The successful synthesis of these high-entropy ABO_3 perovskites reveals the possibility to create high-entropy cubic ceramics and to discover new materials in ABO_3 perovskites family.

Chapter 1. Introduction

1.1. ABO_3 perovskites

Perovskite is a very common structure in ceramics; the general chemistry formula can be described as ABO_3. As is shown in Figure 1.1 (a), the perovskite structure has eight A cations (normally larger than B cations) in the corner, six O anions in the face center, and one B cation in the body center. The A cations are 12-fold coordinated and the B cations are 6-fold coordinated within the oxygen octahedral [1]. In the other way, in Figure 1.1 (b), the structure of ABO_3 perovskites can be viewed as corner sharing BO_6 octahedras, where the A cations are in the center. Usually, in the structure of ABO_3, the candidates for A cations are alkaline earth metal, alkali, or even rare earth metal elements, meanwhile the candidates for B cations are metallic transition metal elements. In 1926, a new concept called "tolerance factor" was put forward by Goldschmidt [2] in order to predict the structure and stability of perovskites, which is defined by the following:

$$t = \frac{R_A + R_O}{\sqrt{2}((R_B) + R_O)}, \tag{1.1}$$

where R_A is the ionic radius of A cation, R_B is the ionic radius of B cation, and R_O is the ionic radius of oxygen anion. The concept of Goldschmidt's tolerance factor is based on the structure of ideal cubic ABO_3 perovskites, where all the ions are touching with each other, so that the geometry relationship can be given as:

$$\sqrt{2}((R_B) + R_O) = R_A + R_O, \tag{1.2}$$

In fact, for most of ABO_3 perovskites, the relationship in Eq. (1.2) cannot be satisfied exactly. However, they still have a cubic structure and some distortion in lattice. A relatively large or small value of tolerance factor can change the structure of ABO_3 to

tetragonal, hexagonal, or rhombohedral instead of cubic. The range of tolerance factor that can form a perovskite structure is between 0.75 and 1.0. When tolerance factor t is smaller than 0.75, the distortion in lattice can change the unit cell in the structure to orthorhombic as is observed in $GdFeO_3$. A hexagonal structure can be formed if t is larger than 1.0 because the BO_6 octahedra starts to share faces instead of sharing corners as is seen for $BaNiO_3$ [3]. In 2008, Li et al. put forward a new concept, octahedral factor (μ) which is given by:

$$\mu = \frac{R_B}{R_X}, \tag{1.3}$$

to predict the structure of ABX_3 (X=F, Cl, Br, I) halide perovskites, so the octahedral factor (μ) can also be considered for ABO_3 perovskites, if the R_X in Eq. (1.3) is substituted with R_O [4]. The combination of Goldschmidt's tolerance factor (t) and octahedral factor (μ) can be taken into account when considering the formability and structure stability of ABO_3 perovskites.

1.2. Applications of ABO_3 perovskites

1.2.1. Solid-oxide fuel cells (SOFCs)

Many ABO_3 perovskites can be used as cathode materials in solid-oxide fuel cells (SOFCs) for their high electronic conductivity, stable thermal property, and good compatibility to work with SOFCs electrolyte, such as $LaMnO_3$, $LaFeO_3$, and $LaCoO_3$[5]. Moreover, Sr dopants in these cathode ABO_3 materials are favored because of their high electronic conductivity in oxidizing atmospheres [6]. Other doped perovskites, for example $SrZr_{0.9}Sc_{0.1}O_3$, were investigated for their potential application on reduced-

temperature electrolytes. Therefore, varieties of ABO_3 structure materials are still very promising in SOFC area [5].

1.2.2. Photodecomposition of water

To date, water splitting has risen a lot of concerns in solving the problem of energy depletion [7-9]. In 1975, $SrTiO_3$ was reported by Wrighton et al. [10] to have the potential to decompose water under solar irradiation into oxygen and hydrogen because of its suitable band gap value of 3.2 eV. Recently, co-catalyst of $NiO/SrTiO_3$ has been discovered to significantly enhance the effects of photodecomposition performance of water, inspiring the deep investigation in this area [11].

1.2.3. Giant dielectric constant

Recently, Nb and Zr Doped $SrTiO_3$ have been reported to have a giant permittivity. Therefore, these kinds of materials are good candidates for sensors and large bypass capacitors. The giant permittivity phenomenon results from the formation of Nb^{5+}, creating cation vacancies (V''_{Sr}) and excessive oxygen ions, forming defects dipoles (V''_{Sr} - $V^{\cdot\cdot}_{O}$), and partial reduction of Ti^{4+} to Ti^{3+} ($Ti^{4+}\cdot$ e), generating giant dipoles with fully ionized oxygen vacancies ($Ti^{4+}\cdot$ e - $V^{\cdot\cdot}_{O}$ - $Ti^{4+}\cdot$ e) [12-14].

1.3. Concept of high-entropy alloys and high-entropy perovskites

High-entropy alloys (HEAs) can be loosely defined as a solid solution that contains five or more than five equal or near equal atomic percent of principal elements [15]. There are four essential effects in high-entropy alloys (HEAs): 1. high-entropy effects, which can stabilize the phases in high-entropy alloys (HEAs); 2. sluggish diffusion effects, where the diffusion rate in HEAs are relatively lower than in stainless steels and pure metals; 3. severe lattice distortion effects, which results in the high

strength of HEAs; 4. cocktail effects, where unexcepted properties that any single element doesn't have can be achieved [16]. To date, varieties of HEAs that have promising properties have been discovered, such as the high hardness and good fatigue behavior of $Al_{0.5}CoCrCuFeNi$ [17, 18] and the high wear-resistance of $Co_{1.5}CrFeNi_{1.5}Ti$ and $Al_{0.2}Co_{1.5}CrFeNi_{1.5}Ti$ [15, 19].

According to the Gibbs phase rule at constant pressure, which is given by:

$$F = C-P+1, \tag{1.4}$$

where F is the degree of freedom in the system, equals to zero at equilibrium, C is the number of components, and P is the number of phases that can exist. For a high-entropy system with five components, six phases can exist in maximum at equilibrium. However, for most of HEAs, the existing phases are much less than the maximum number from the Gibbs phase rule. This suggests that the mixing of components increases the solubility between each single element due to the high configurational entropy and sluggish diffusion of atoms. This mixing effects can bring significantly promising properties, such as high hardness, high strength, and high corrosion resistance, which are discovered and controlled.

In the 1870's, an equation to calculate the configurational entropy was developed by Ludwig Boltzmann [20], which is given by:

$$\Delta S_{conf} = k \ln w, \tag{1.5}$$

where k = 1.38×10^{-23} J/K is Boltzmann's constant, w is the total number of possible micro-states corresponding to the macro-states of the system. Therefore, the configurational entropy of high-entropy system can be developed as:

$$\Delta S_{conf} = -R \sum_{i=1}^{n} X_i \ln X_i = R \ln N, \tag{1.6}$$

where R=8.314 J/(K·mol) is gas constant, X_i is the mole fraction for the ith elements, and N is the number of components. Thus, Eq. (1.6) suggests that the configurational entropy of a system with five equal mole compositions, ΔS_{conf}= 1.61R, is larger than that with four equal mole compositions, ΔS_{conf}= 1.39R. At high temperature, according to the Gibbs free energy equation:

$$\Delta G = \Delta H - T\Delta S, \tag{1.7}$$

higher configurational entropy leads to lower Gibbs free energy and enhances the system stability.

Recently, a crystalline entropy-stabilized oxide, $Mg_{0.2}Ni_{0.2}Co_{0.2}Cu_{0.2}Zn_{0.2}O$, was successfully synthesized via high temperature quenching experiments by Rost et al. [21], inspiring the idea of creating high-entropy oxides. Following that work, David et al. [22] discovered the high dielectric constant in modified high-entropy oxides; for example, $(MgCoNiCuZn)_{1-x}Li_xO$, $(MgCoNiCuZn)_{1-2x}(LiGa)_xO$, and $(MgCoNiCuZn)_{0.8}(LiGa)_{0.2}O$ based on the idea of Rost. Subsequently, seven equimolar high-entropy homogeneous diborides with five components were successfully synthesized by Gild et al. [23], where these noncubic (hexagonal) high-entropy diborides ceramics were shown to have high hardness and good oxidation resistance at high temperature. The concept of high-entropy perovskites is based on the concept of high-entropy alloys (HEAs) and the structure of ABO_3 perovskites, as the four core effects of high-entropy alloys (HEAs) may also exist in high-entropy ceramics. In an ABO_3 perovskite structure, there are two cations, so both can be substituted and a large variety of combinations are available. Therefore, some very promising properties can also be achieved because of the enormous total number of possible combinations. In this research, we substituted the B sites with five kinds of

elements for most of the cases. Six, out of eleven, equal mole compositions, #S1, $Sr(Zr_{0.2}Sn_{0.2}Ti_{0.2}Hf_{0.2}Mn_{0.2})O_3$, #S5, $Sr(Zr_{0.2}Sn_{0.2}Ti_{0.2}Hf_{0.2}Nb_{0.2})O_3$, #B2, $Ba(Zr_{0.2}Sn_{0.2}Ti_{0.2}Hf_{0.2}Ce_{0.2})O_3$, #B3, $Ba(Zr_{0.2}Sn_{0.2}Ti_{0.2}Hf_{0.2}Y_{0.2})O_{3-x}$, #B5, $Ba(Zr_{0.2}Sn_{0.2}Ti_{0.2}Hf_{0.2}Nb_{0.2})O_3$, and #BS1, $(Ba_{0.5}Sr_{0.5})(Zr_{0.2}Sn_{0.2}Ti_{0.2}Hf_{0.2}Nb_{0.2})O_3$, of homogeneous single phase ABO_3 perovskites were synthesized. The successful synthesis of these high-entropy ABO_3 perovskites shows a new method to create new class of materials in ABO_3 perovskites family.

Chapter 2. Experiment procedure and equipment

2.1. Selection of atoms

The candidates of atoms are shown in Figure 2.1. The candidates for A sites are marked with yellow circle and the candidates for B sites are marked with green circles. For A atoms and B atoms in ABO_3 structure, there are three kinds of possible combinations, $A^{+}B^{5+}$, $A^{3+}B^{3+}$, and $A^{2+}B^{4+}$ based on the valence of O atom. However, in this thesis, we only consider the $A^{2+}B^{4+}$ case which is more common and has more possible combinations. The reason why I chose these atoms is basically based on the ionic radius. The closer the ionic radius of these atoms the less lattice distortion it maintains in the structure, partially stabilizing the finally structure.

2.2. Experiment procedure

2.2.1. Preparation of high-entropy perovskites

The starting powders are SrO (99.5%, metals basis, from Alfa Aesar Inc., USA), $SrTiO_3$ (>99%, metals basis, from Alfa Aesar Inc., USA), $SrSnO_3$ (99%, from Alfa Aesar Inc., USA), HfO_2 (99%, metals basis, from Alfa Aesar Inc., USA), $SrZrO_3$ (99.3%, metals basis, from Alfa Aesar Inc., USA), GeO_2 (>99.99%, trace metals basis, from Sigma-Aldrich Inc., USA), MnO_2 (99.9%, metals basis, from Alfa Aesar Inc., USA), Y_2O_3 (99.99%, trace metals basis, from Sigma-Aldrich Inc., USA), NbO_2 (99.9%, trace metals basis, from Sigma-Aldrich Inc., USA), CeO_2 (99.9%, metals basis, from Alfa Aesar Inc., USA), BaO (99.5%, metals basis, from Alfa Aesar Inc., USA), $BaZrO_3$ (99%, metals basis, from Alfa Aesar Inc., USA), $BaTiO_3$ (99.5%, trace metals basis, from Sigma-Aldrich Inc., USA), SnO_2 (99.9%, trace metals basis, from Sigma-Aldrich Inc., USA). The raw powders were appropriately weighed based on the stoichiometric mole

fraction, so that high-entropy ABO_3 perovskites with five equal mole fraction of atoms in B site can be reached. The detailed compositions are shown in Table 2.1.

The raw powders were hand mixed and high energy ball milled in a Si_3N_4 container via Spex 8000D (SpexCertPrep, USA) for six hours. The high energy ball milling process included 12 cycles, and in order to prevent overheating, the powders were ball milled for 30 minutes and stopped for 10 minutes to cool down in each cycle. Post milling, mixed powders were compacted into pellets in a 1/4 inch die with the pressing pressure of 300 MPa and holding for 120 seconds. The pellets were sintered in a high temperature tube furnace (GSL-1700X, MTI Inc., USA) at 1100 °C, 1300 °C, 1400 °C, and 1500 °C separately with the heating rate of 5 °C per minute, a holding time of 10 hours, and were cooled naturally to room temperature.

2.2.2. Characterization

X-ray diffraction (XRD) patterns were obtained with a Rigaku diffractometer with a Cu Kα radiation from 20° to 80°, with a step of 0.02 °/s. Scanning electron microscopy (SEM, Phillips XL30, FEI Inc.) was used to verify the phase purity by energy dispersive X-ray spectroscopy (EDS) mapping. Dual-beam FIB/SEM (Scios, FEI Inc.) was used to prepare TEM samples. Aberration-corrected scanning transmission electron microscopy (AC STEM) was utilized to preform characterization on samples in nanoscale. STEM high-angle annular dark-field (HAADF) graphs and STEM annular bright-field (ABF) graphs were conducted by STEM (ARM-200F, JEOL Inc., USA) with a voltage of 200 kV.

Chapter 3. Results and discussion

In this chapter, two compositions of Ba and Sr system with four kinds of atoms in B sites, and eleven compositions of Ba and Sr system with five kinds of atoms in B sites are discussed. The phase stability of high-entropy perovskites and the possible key factors to form a homogeneous single phase are also included. XRD was preformed to discover the structure of all samples and EDS mapping images were used to verify the homogeneity of each element in all compositions. STEM-HAADF and STEM-ABF images were taken to characterize composition #S1, $Sr(Zr_{0.2}Sn_{0.2}Ti_{0.2}Hf_{0.2}Mn_{0.2})O_3$, in nanoscale. Air quench experiments were carried out to prove the phase stability of composition #S1 as well. Goldschmidt's tolerance factor (t) and lattice parameter (a) were also calculated from theoretical models. Possible peak intensity of all compositions in XRD patterns were calculated by equation:

$$I = |F_{hkl}|^2 p_{hkl} L_p(\theta) A(\theta) e^{-2M}, \quad (3.1)$$

where

Structure factor: $F_{hkl} = \sum_{n=1}^{N} f_n e^{2\pi i(h\mu_n + kv_n + lw_n)}$, (3.2)

Scatting factor: $f_n(s) = Z - 41.8214 \times s^2 \times \sum_{i=1}^{N} a_i e^{-b_i s^2}$, (3.3)

$s = \frac{\sin(\theta)}{\lambda}$, (3.4)

Multiplicity factor: p_{hkl},

Lorentz factor: $L_p(\theta) = \frac{1+cos^2 2\theta}{sin^2\theta \cos\theta}$, (3.5)

Absorption factor: $A(\theta)$ (assume it is unity),

Temperature factor: e^{-2M} (assume it is unity),

$M = B(\frac{\sin\theta}{\lambda})^2$, (3.6)

Possible positions of all compositions in XRD pattern were calculated by Bragg's law:

$$2d\sin\theta=n\lambda, \quad (3.7)$$

3.1. Ba and Sr system with four kinds of atoms in B sites

The Ba and Sr system with four kinds of atoms in B sites were synthesized in order to test the possibility of making high-entropy ABO_3 perovskites with five atoms in B sites. Figure 3.1 and Figure 3.2 show the XRD pattern of $Sr(Zr_{0.25}Sn_{0.25}Ti_{0.25}Hf_{0.25})O_3$ and $Ba(Zr_{0.25}Sn_{0.25}Ti_{0.25}Hf_{0.25})O_3$ at 1100 °C, 1300 °C, and 1500 °C, respectively. Both figures show the trend that at low temperature, XRD patterns show more than one major phase; however, with the increase of temperature from 1100 °C to 1500 °C, the peaks have the potential to merge into one major phase. This phenomenon results from the fact that for almost every pure single phase perovskite, even those that have different structures at room temperature, becomes a cubic structure at high temperature with the space group of $Pm\bar{3}m$. Figure 3.3 shows some of the structure changes of different perovskites with the increase of temperature. Although the temperature is as high as 1500 °C, these two kinds of compositions cannot form a single phase, where the shoulders of the peaks are very apparent and the unknown secondary phases are marked as star. However, these promising results give us the potential possibility of synthesizing high-entropy ABO_3 perovskites with five kinds of atoms in B sites.

3.2. Sr system with five kinds of atoms in B sites

Based on the results of Sr system with four kinds of atoms in B sites, Sr systems with five kinds of atoms in B sites were investigated. The selection of atoms was discussed in chapter 2.

3.2.1. $Sr(Zr_{0.2}Sn_{0.2}Ti_{0.2}Hf_{0.2}Mn_{0.2})O_3$

Figure 3.4 shows the XRD pattern of composition #S1, $Sr(Zr_{0.2}Sn_{0.2}Ti_{0.2}Hf_{0.2}Mn_{0.2})O_3$, at 1300 °C, 1400 °C, and 1500 °C. The secondary phases are marked as star. Obvious secondary phases can be seen at 1300 °C. However, at 1400 °C and 1500 °C, the XRD patterns display a cubic phase with the lattice constant (a) of 3.992 Å, which is close to the calculation of empirical formula for composition #S1 4.032 Å, and there is no trace of secondary phases from the XRD pattern. Furthermore, the red bars in the bottom of the image show potential positions of peaks and intensity by calculation. Figure 3.5 (a) and 3.5 (b) are the EDS results of composition #S1 at 1400 °C and 1500 °C, respectively. At 1400 °C, apparent precipitation of Mn enriched phase was detected from the EDS mapping results. The EDS mapping results show that it is a homogeneous single phase at 1500 °C.

STEM ABF and HAADF were carried out to verify that composition #S1 formed a cubic ABO_3 perovskite structure at 1500 °C in nanoscale. The STEM ABF and STEM HAADF images in Figure 3.6 (a) and Figure 3.6 (b) show the arrangement of atoms in composition #S1 at 1500 °C. Higher magnification images are presented in Figure 3.6 (c), where the $[00\bar{1}]$ zone axis and two perpendicular atomic planes (110) and $(\bar{1}10)$ are marked in red. The average d spacing of two (001) plane is about 4.010 Å, which is very close to the calculation results from the XRD pattern 3.992 Å. Figure 3.6 (d) shows the position of each atoms, where the A atoms are marked in green, the B atoms are marked in blue, and the O atoms are marked in red. The O atoms cannot be clearly seen in Figure 3.6 (d) because of its low atomic number (Z). In the STEM-HAADF images, the intensity of atoms is proportional to $Z^{1.7}$ (Z^2 is theoretical value), where Z is the atomic number of the atoms [24]. Table 3.1 shows the values of $Z^{1.7}$ for all elements in the case of

composition #S1. While $Z_{Mn}^{1.7}$ = 238 and $Z_{Ti}^{1.7}$ = 191 are smaller than $Z_{Sr}^{1.7}$ = 485, all the other elements in the B sites have a $Z^{1.7}$ value larger than $Z_{Sr}^{1.7}$, so the B atoms show a higher intensity. This is observed in the results in Figure 3.6 (d). Therefore, the composition #S1 can be viewed as a homogeneous and uniform single phase high-entropy ABO_3 solid solution and its atomic structure is thoroughly consistent with the cubic structure depicted in Figure 1.1 (a).

Air quench experiments were conducted to investigate the phase stability of composition #S1 at different temperatures. A sample was sintered at 1500 °C for 2 hours and then air quenched to room temperature. Similarly, a sample was sintered at 1500 °C for 2 hours, then held at 1400 °C for 2 hours, and quenched to room temperature. These samples yielded the EDS mapping results in Figure 3.7 (a) and 3.7 (b), respectively. They display that composition #S1 is a uniform single phase at 1500 °C but there are some Mn enriched secondary phases at 1400 °C. Combined with the EDS results in Figure 3.5 (a), conclusions can be made that the single phase of composition #S1 is entropy stabilized and Mn enriched secondary phases are precipitated below 1400 °C.

3.2.2. $Sr(Zr_{0.2}Sn_{0.2}Ti_{0.2}Hf_{0.2}Ce_{0.2})O_3$

Figure 3.8 represents the XRD pattern of composition #S2, $Sr(Zr_{0.2}Sn_{0.2}Ti_{0.2}Hf_{0.2}Ce_{0.2})O_3$, at 1300 °C, 1400 °C, and 1500 °C. The secondary phases are marked as star. Obvious secondary phases can be seen at all temperature. However, with the increase of temperature, the XRD patterns display that the peaks evolve into one major cubic perovskite phase. Likewise, the potential positions and intensity of #S2 by calculation, which is represented by red bars, are consistent with the peaks of major cubic

phase in the XRD pattern. Thus, composition #S2 did not form a homogeneous single phase at 1300 °C, 1400 °C, and 1500 °C.

3.2.3. $Sr(Zr_{0.2}Sn_{0.2}Ti_{0.2}Hf_{0.2}Y_{0.2})O_{3-x}$

Figure 3.9 displays the XRD pattern of composition #S3, $Sr(Zr_{0.2}Sn_{0.2}Ti_{0.2}Hf_{0.2}Y_{0.2})O_{3-x}$, at 1300 °C, 1400 °C, and 1500 °C. The secondary phases are marked as star. There are minor secondary phases at 1300 °C, 1400 °C, and 1500 °C. The XRD peaks in the major phase are not symmetric and apparent shoulders can be found, representing the inhomogeneity of this composition, but the major phase is a cubic structure. More evidence can be achieved from the EDS results in Figure 3.5 (c) that Y enriched secondary phases precipitated at 1500 °C. Therefore, composition #S3 cannot form a homogeneous single phase at 1300 °C, 1400 °C, and 1500 °C.

3.2.4. $Sr(Zr_{0.2}Sn_{0.2}Ti_{0.2}Hf_{0.2}Ge_{0.2})O_3$

Figure 3.10 shows the XRD pattern of composition #S4, $Sr(Zr_{0.2}Sn_{0.2}Ti_{0.2}Hf_{0.2}Ge_{0.2})O_3$, at 1300 °C, 1400 °C, and 1500 °C, where the major phases of each temperature is a cubic structure. The secondary phases are marked as star. Perhaps due to the fast scanning speed, at 1300 °C there is no trace of secondary phases in XRD patterns, whereas, with the increase of temperature to 1500 °C, a large quantity of secondary phases can be seen from the XRD pattern. However, the EDS results in Figure 3.5 (d) reveal that there are some precipitations of Ge enriched phases at 1300 °C, so composition #S4 is very unlikely to form a homogeneous single phase.

3.2.5. $Sr(Zr_{0.2}Sn_{0.2}Ti_{0.2}Hf_{0.2}Nb_{0.2})O_3$

Figure 3.11 represents the XRD pattern of composition #S5, $Sr(Zr_{0.2}Sn_{0.2}Ti_{0.2}Hf_{0.2}Nb_{0.2})O_3$, at 1300 °C, 1400 °C, and 1500 °C. Secondary phases can

be found at 1300 °C, which are marked as star. At 1400 °C and 1500 °C, the XRD patterns show a cubic phase with the lattice constant (a) of 4.021 Å, close to the results of empirical formula 4.067 Å. The potential positions of peaks and intensity by calculation and the plane index are shown at the bottom of the image. The homogeneity of composition #S5 at 1500 °C was verified by the measurements of EDS mapping, and the EDS results in Figure 3.5 (e) show that there is no trace of secondary phases and all elements are uniform for composition #S5 at 1500 °C. Therefore, composition #S5 can form a uniform and homogeneous cubic structure solid solution at 1500 °C.

3.3. Sr system with five kinds of atoms in B sites

Based on the results of Ba system with four kinds of atoms in B sites, Ba systems with five kinds of atoms in B sites was investigated. The selection of atoms was discussed in chapter 2.

3.3.1. $Ba(Zr_{0.2}Sn_{0.2}Ti_{0.2}Hf_{0.2}Mn_{0.2})O_3$

Figure 3.12 represents the XRD pattern of composition #B1, $Ba(Zr_{0.2}Sn_{0.2}Ti_{0.2}Hf_{0.2}Mn_{0.2})O_3$, at 1300 °C, 1400 °C, and 1500 °C. The secondary phases are marked as star. At 1300 °C and 1400 °C, there are only a small quantity of secondary phases, however, with the increase of temperature to 1500 °C, apparent secondary phases can be found from the XRD pattern. More EDS measurements were conducted to find that the Mn enriched secondary phases precipitated at 1500 °C in Figure 3.13 (a). Therefore, composition #B1 cannot form a uniform and homogeneous single phase at any of the temperatures investigated.

3.3.2. $Ba(Zr_{0.2}Sn_{0.2}Ti_{0.2}Hf_{0.2}Ce_{0.2})O_3$

Figure 3.14 shows the XRD pattern of composition #B2, $Ba(Zr_{0.2}Sn_{0.2}Ti_{0.2}Hf_{0.2}Ce_{0.2})O_3$, at 1300 °C, 1400 °C, and 1500 °C. The secondary phases of CeO_2 are marked as star. There is no trace of secondary phase from the XRD pattern at 1300 °C and the peak positions and intensity give a cubic perovskite, however, obvious secondary phases can be found at 1400 °C and 1500 °C. Furthermore, with the increase of temperature the peak intensity of secondary phases becomes higher. Compared with the database from ICSD, the secondary phases can be confirmed as CeO_2. More evidence can be achieved from the EDS mapping data in Figure 3.13 (b) which shows that only Ce enriched phase precipitated, whereas other elements are homogeneous, which is consistent with the XRD results. Another EDS mapping results in Figure 3.13 (c) reveals that every element in composition #B2 at 1300 °C is uniform and homogeneous. The calculation of lattice parameter (a) of composition #B2 at 1300 °C is 4.192 Å, which is very close to the results of empirical formula 4.198 Å. To sum up, Composition #B2 can form a uniform and homogeneous cubic perovskite phase at 1300 °C.

3.3.3. $Ba(Zr_{0.2}Sn_{0.2}Ti_{0.2}Hf_{0.2}Y_{0.2})O_{3-x}$

Figure 3.15 is the XRD pattern of composition #B3, $Ba(Zr_{0.2}Sn_{0.2}Ti_{0.2}Hf_{0.2}Y_{0.2})O_{3-x}$, at 1300 °C, 1400 °C, and 1500 °C. The secondary phases are marked as star. There is no trace of secondary phase in the XRD pattern at 1300 °C and the peak positions and intensity give a cubic perovskite. A large quantity of secondary phases can be found at 1400 °C and 1500 °C. EDS mapping graphs presented in Figure 3.13 (d) show that composition #B3, $Ba(Zr_{0.2}Sn_{0.2}Ti_{0.2}Hf_{0.2}Y_{0.2})O_{3-x}$, is a uniform and homogeneous single phase. Besides, the calculation result of lattice parameter (a) of composition #B3 at 1300 °C is 4.179 Å, which matches with the empirical formula 4.205 Å.

3.3.4. $Ba(Zr_{0.2}Sn_{0.2}Ti_{0.2}Hf_{0.2}Ge_{0.2})O_3$

Composition #B4, $Ba(Zr_{0.2}Sn_{0.2}Ti_{0.2}Hf_{0.2}Ge_{0.2})O_3$, was sintered at 1300 °C, 1400 °C, and 1500 °C and the XRD patterns were shown in Figure 3.16. Secondary phases which are marked as star can be seen clearly at all three temperatures. Besides, the peak around 31 degree is not symmetric revealing that this composition is not a single phase. Thus, composition #B4 cannot form a uniform single phase at 1300 °C, 1400 °C, and 1500 °C.

3.3.5. $Ba(Zr_{0.2}Sn_{0.2}Ti_{0.2}Hf_{0.2}Nb_{0.2})O_3$

The XRD pattern of composition #B5, $Ba(Zr_{0.2}Sn_{0.2}Ti_{0.2}Hf_{0.2}Nb_{0.2})O_3$, at 1300 °C, 1400 °C, and 1500 °C is presented in Figure 3.17, where the secondary phases are marked as star. A uniform XRD pattern of cubic perovskite is shown at 1300 °C, and there is no trace of secondary phases at all. However, secondary phases appear at 1400 °C and with the increase of temperature, the peak intensity of secondary phases increases. EDS mapping results are shown in Figure 3.13 (e), where all the elements in this composition are homogeneous and uniform. From the XRD pattern, lattice parameter (a) is also calculated as 4.104 Å which is very close to the results of empirical formula, 4.155 Å. Based on all the experiment results of composition #B5, a conclusion can be made that composition #B5 can form a uniform and homogeneous cubic single phase at 1300 °C.

3.4. $(Ba_{0.5}Sr_{0.5})(Zr_{0.2}Sn_{0.2}Ti_{0.2}Hf_{0.2}Nb_{0.2})O_3$

Due to the promising experiment results of all ten composition above, interest in multiple cations in the A site in addition to the B site was increased. Composition #S5, $Sr(Zr_{0.2}Sn_{0.2}Ti_{0.2}Hf_{0.2}Nb_{0.2})O_3$, can form a homogeneous single phase at 1500 °C, while composition #B5, $Ba(Zr_{0.2}Sn_{0.2}Ti_{0.2}Hf_{0.2}Nb_{0.2})O_3$ can form a uniform single phase at

1300 °C. Whether a single phase with both the Sr and Ba in the A sites would be possible was investigated. The mixing of these two compositions gives a conclusion that the temperature range of forming a single is broadened. Composition #BS1, $(Ba_{0.5}Sr_{0.5})(Zr_{0.2}Sn_{0.2}Ti_{0.2}Hf_{0.2}Nb_{0.2})O_3$ can form a homogeneous single phase at both 1400 °C and 1500 °C. Figure 3.18 is the XRD pattern of composition #BS1 at 1300 °C, 1400 °C, and 1500 °C, where secondary phases are marked as star. At 1300 °C, apparent secondary phases can be found; however, it shows a uniform cubic single phase pattern at both 1400 °C and 1500 °C, where there is no trace of secondary phases. EDS mapping results can be found in Figure 3.19 (a) for 1400 °C and Figure 3.19 (b) for 1500 °C. In both Figure 3.19 (a) and (b), elements are uniform and homogeneous, where no precipitations of elements can be found. The calculation of lattice parameter (a) from the XRD pattern is 4.027 Å, close to the empirical results of 4.111 Å.

3.5. Summary of all compositions

Among the eleven compositions discussed, six compositions can form a homogeneous single phase. These compositions are #S1, $Sr(Zr_{0.2}Sn_{0.2}Ti_{0.2}Hf_{0.2}Mn_{0.2})O_3$, #S5, $Sr(Zr_{0.2}Sn_{0.2}Ti_{0.2}Hf_{0.2}Nb_{0.2})O_3$, #B2, $Ba(Zr_{0.2}Sn_{0.2}Ti_{0.2}Hf_{0.2}Ce_{0.2})O_3$, #B3, $Ba(Zr_{0.2}Sn_{0.2}Ti_{0.2}Hf_{0.2}Y_{0.2})O_{3-x}$, #B5, $Ba(Zr_{0.2}Sn_{0.2}Ti_{0.2}Hf_{0.2}Nb_{0.2})O_3$, and #BS1, $(Ba_{0.5}Sr_{0.5})(Zr_{0.2}Sn_{0.2}Ti_{0.2}Hf_{0.2}Nb_{0.2})O_3$. Table 3.2 is a summary of phase stability and other parameters of all eleven compositions. In this table, single phase samples are marked as ‘Yes’; samples with secondary phases, but cannot be discovered by XRD based on our relatively fast scanning speed, are marked as ‘1’; samples that the intensity of secondary phases is less than 6% are marked as ‘2’; samples that the intensity of secondary phases is more than 6% are marked as ‘3’. Homogeneous single phase can

form at low temperature 1300 °C for Barium based systems, whereas uniform single phase can form at high temperature 1500 °C for Strontium based systems.

The atomic-size difference (δ) and the enthalpy of mixing (ΔH_{mix}) are the two key factors to predict the phase stability of high-entropy alloys (HEAs), where in order to form a stable phase, $\delta < 4\%$ and $\Delta H_{mix} < 5$ KJ/mol are two essential conditions.

$$\delta = \sqrt{\sum_{i=1}^{N} C_i(1 - R_i/(\sum_{i=1}^{N} C_i R_i))^2}, \quad (3.8)$$

$$\Delta H_{mix} = \sum_{i=1, i\neq j}^{N} 4\Delta H_{AB}^{mix} C_i C_j, \quad (3.9)$$

Where R_i is the atomic radius of the ith component; C_i is the mole fraction of ith component; ΔH_{AB}^{mix} is the mixing enthalpy of binary A-B system. Based on the concept of high-entropy alloys (HEAs), δ_{R_B} can also be calculated for high-entropy ABO_3 perovskites using the ionic radius with the coordination number of six. However, ΔH_{mix} cannot be calculated because ΔH_{AB}^{mix} is complicated and unknown in this case. The value of atomic-size different (δ_{R_B}) was calculated at the second last column of table 3.2. However, the criterion of high-entropy alloys (HEAs) cannot extend to high-entropy ABO_3 perovskites because the phase stability of latter is not only dependent on the ionic radius of B atoms, but also related to the ionic radius of A atoms. In the Sr system, both compositions #S1, $Sr(Zr_{0.2}Sn_{0.2}Ti_{0.2}Hf_{0.2}Mn_{0.2})O_3$, and #S4, $Sr(Zr_{0.2}Sn_{0.2}Ti_{0.2}Hf_{0.2}Nb_{0.2})O_3$, have the atomic size difference δ_{R_B} of 8.7%, but only composition #S1 can form a homogeneous single phase. Compared with the Ba system and Sr system the δ_{R_B} of both composition #S1, $Sr(Zr_{0.2}Sn_{0.2}Ti_{0.2}Hf_{0.2}Mn_{0.2})O_3$, and #B1, $Ba(Zr_{0.2}Sn_{0.2}Ti_{0.2}Hf_{0.2}Mn_{0.2})O_3$, is 8.7%, and the former can form a homogeneous single phase, but the latter does not. Likewise, compositions #S2, $Sr(Zr_{0.2}Sn_{0.2}Ti_{0.2}Hf_{0.2}Ce_{0.2})O_3$,

and #S3, $Sr(Zr_{0.2}Sn_{0.2}Ti_{0.2}Hf_{0.2}Y_{0.2})O_{3-x}$, do not form a uniform single phase, but compositions #B2, $Ba(Zr_{0.2}Sn_{0.2}Ti_{0.2}Hf_{0.2}Ce_{0.2})O_3$, and #B3, $Ba(Zr_{0.2}Sn_{0.2}Ti_{0.2}Hf_{0.2}Y_{0.2})O_{3-x}$ can, though they have the same δ_{R_B}, respectively. However, both #S5, $Sr(Zr_{0.2}Sn_{0.2}Ti_{0.2}Hf_{0.2}Nb_{0.2})O_3$, and #B5, $Ba(Zr_{0.2}Sn_{0.2}Ti_{0.2}Hf_{0.2}Nb_{0.2})O_3$, can form a homogeneous single phase with a relatively small δ_{R_B} of 4.8%. In conclusion, the criterion of high-entropy alloys (HEAs) is not that applicable for high-entropy ABO_3 perovskites, but a relatively small value of δ_{R_B} (δ_{R_B} < 5%) is favored to form a stable homogeneous single phase.

A criterion called Goldschmidt tolerance factor, which is very common in single component perovskites, is introduced for the purpose of predicting phase stability of high-entropy ABO_3. The factor is based on the ionic radius of A atoms and B atoms, so both the effects of A and B atoms are considered, where in the case of high-entropy of ABO_3 perovskites an average R_B ($\overline{R_B}$) was utilized. The value of tolerance factor (t) is presented at the last column of table 3.2. The formula of tolerance factor (t) is shown below:

$$t = \frac{R_A + R_O}{\sqrt{2}(\overline{R_B}) + R_O)}, \tag{3.10}$$

For a single component ABO_3 perovskites, a cubic structure can be formed when the tolerance factor (t) is between 0.9 and 1.0, while a hexagonal or tetragonal structure can form when t is larger than 1.0 and if t is smaller than 0.9, orthorhombic or rhombohedral structure can from [3].

In the case of high-entropy ABO_3 perovskites, based on the data of tolerance factor (t) and the phase stability of all compositions, compositions that have a tolerance

factor (t) closer to 1.0, which is the tolerance factor of an ideal cubic perovskite, have more possibility to form a homogeneous single phase than those are further away from 1.0. For example, composition #S1, $Sr(Zr_{0.2}Sn_{0.2}Ti_{0.2}Hf_{0.2}Mn_{0.2})O_3$, #S5, $Sr(Zr_{0.2}Sn_{0.2}Ti_{0.2}Hf_{0.2}Nb_{0.2})O_3$, #B2, $Ba(Zr_{0.2}Sn_{0.2}Ti_{0.2}Hf_{0.2}Ce_{0.2})O_3$, #B3, $Ba(Zr_{0.2}Sn_{0.2}Ti_{0.2}Hf_{0.2}Y_{0.2})O_{3-x}$, #B5, $Ba(Zr_{0.2}Sn_{0.2}Ti_{0.2}Hf_{0.2}Nb_{0.2})O_3$, and #BS1, $(Ba_{0.5}Sr_{0.5})(Zr_{0.2}Sn_{0.2}Ti_{0.2}Hf_{0.2}Nb_{0.2})O_3$, have the tolerance factor (t) of 0.99, 0.97, 1.01, 1.03, and 1.00 respectively, while composition #S2, $Sr(Zr_{0.2}Sn_{0.2}Ti_{0.2}Hf_{0.2}Ce_{0.2})O_3$, #S3, $Sr(Zr_{0.2}Sn_{0.2}Ti_{0.2}Hf_{0.2}Y_{0.2})O_{3-x}$, #B1, $Ba(Zr_{0.2}Sn_{0.2}Ti_{0.2}Hf_{0.2}Mn_{0.2})O_3$, #B4, $Ba(Zr_{0.2}Sn_{0.2}Ti_{0.2}Hf_{0.2}Ge_{0.2})O_3$, have the tolerance factor (t) of 0.95, 0.95, 1.05, 1.05 respectively. However, there is an exception that composition #S4, $Sr(Zr_{0.2}Sn_{0.2}Ti_{0.2}Hf_{0.2}Ge_{0.2})O_3$, has a tolerance factor (t) of 0.99, which is close enough to 1.0, but still cannot form a single phase. Therefore, an appropriate value of tolerance factor (t) is a necessary, but not sufficient, condition to form a single phase. In the other way, samples that cannot form a single phase, except composition #S4, all have a tolerance factor (t) smaller than 0.97 or larger than 1.04. This is mainly attributed to the fact that a relatively large or small tolerance factor can influence the structure of perovskites. As was mentioned previously, the influence of the value of tolerance factor (t) on the structure of one component ABO_3 perovskites can also extend to high-entropy ABO_3 perovskites. Even if this ionic radius of B atom in the tolerance factor is calculated by the average number of the five B atoms ($\overline{R_B}$), tolerance factor (t) can still give a trend of whether a single phase can form, because relatively large or small t can make the cubic structure, the major phase in all eleven compositions, not stable and have the possibility to transform to another structure. Table 3.3 is another summary table of all the

compositions that can form a single phase. The empirical formula of lattice parameter [25, 26] is shown below:

$$a = 1.8836(R_A+R_O)+1.4898t-1.2062, \quad (3.11)$$

where t is the tolerance factor which is mentioned before. In this table, lattice parameter (a) from XRD pattern and from empirical formula are compared, and the values from these two different methods are very close, with an error margin smaller than 1.3%. This relatively small value of error can partially verify the feasibility of using average number of R_B ($\overline{R_B}$) instead of R_B in the case of high-entropy perovskites.

In conclusion, Goldschmidt's tolerance factor (t) is proved to be a necessary, but not sufficient, condition to form a homogeneous single phase, whereas the revised Hume-Ruthery rule for high-entropy alloys (HEAs) can not extend to the case of high-entropy ABO_3 perovskites. The mixing of two compositions, which can form a homogeneous single phase separately, broadens the temperature range of forming a uniform solid solution. Besides, for Ba system single phase formed at low temperature (1300 °C), whereas for Sr system single phase formed at high temperature (1500 °C).

Chapter 4. Suggested future work

There is a large amount of potential for future research due to the large compositional space. More compositions can be tested and some theoretical calculations can be carried out.

4.1. Mixing of Ba system and Sr system

Composition #BS1, $(Ba_{0.5}Sr_{0.5})(Zr_{0.2}Sn_{0.2}Ti_{0.2}Hf_{0.2}Nb_{0.2})O_3$ is a mix of composition #S5, $Sr(Zr_{0.2}Sn_{0.2}Ti_{0.2}Hf_{0.2}Nb_{0.2})O_3$ and #B5, $Ba(Zr_{0.2}Sn_{0.2}Ti_{0.2}Hf_{0.2}Nb_{0.2})O_3$, while the temperature range to form a single is broadened after mixing. It would be very interesting to see whether the mixing of other two compositions in Ba system and Sr system can make it possible to form a homogeneous single phase, despite one of them not forming a single phase on its own.

4.2. Improvement of relative density

The relative density of all the samples are between 70% and 87%, which is a relatively low value. In order to get good results of property measurement, nearly fully dense samples are ideal. Samples after sintering did not reach an idea density because the sintering method is only conventional sintering. Spark plasma sintering (SPS) method was also tried to get a sample with high density; however, the valence change of Ti^{4+} results in secondary phases and the contamination of carbon can be another problem.

4.3. Density functional theory (DFT)

DFT simulation can be conducted to calculate the band gap of all compositions that can form a single phase. Compared with traditional ABO_3 perovskite material, high-entropy perovskites have five kinds of different atoms in B sites, where it gives more

possibilities to coordinate atoms in B sites in order to improve the value of band gap to the target results based on applications.

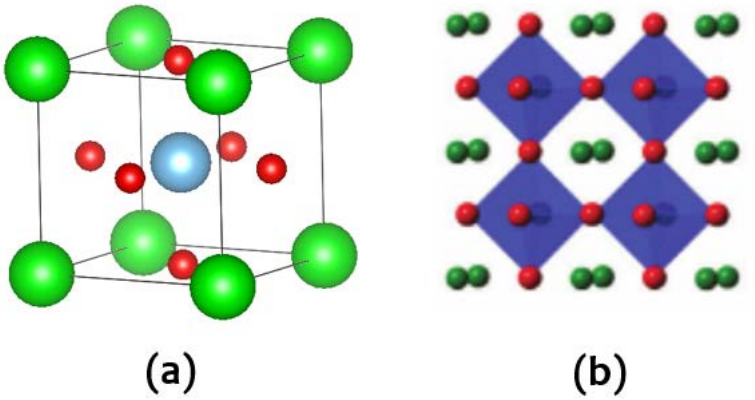

Figure 1.1 Structure of ABO_3 Perovskites [11].

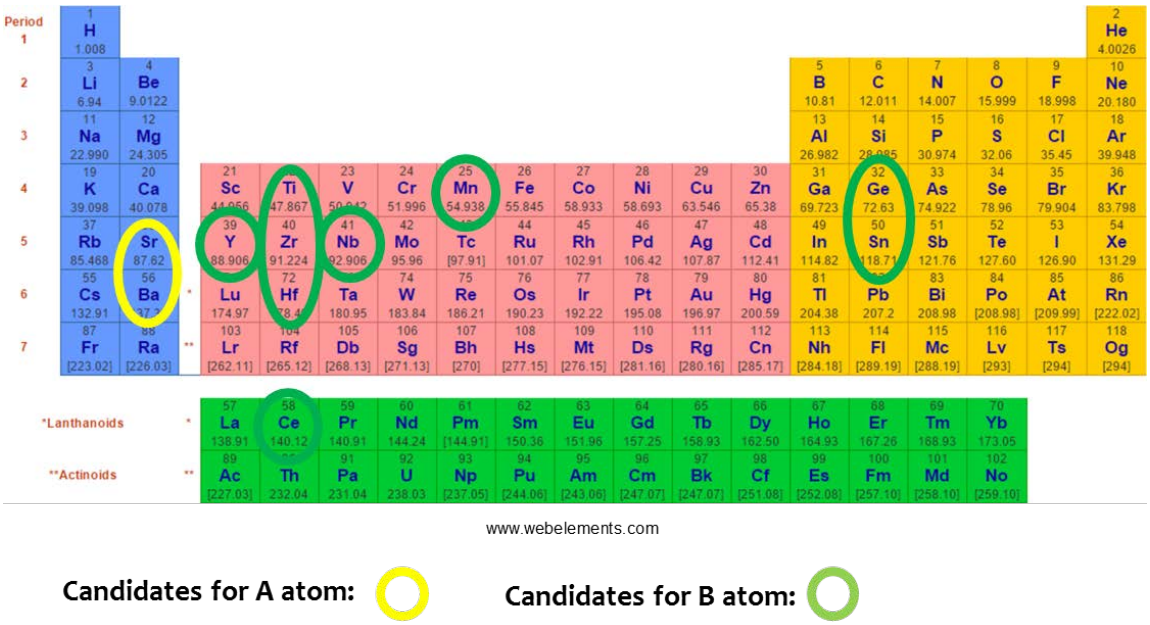

Figure 2.1 Candidate atoms for ABO_3 perovskites.

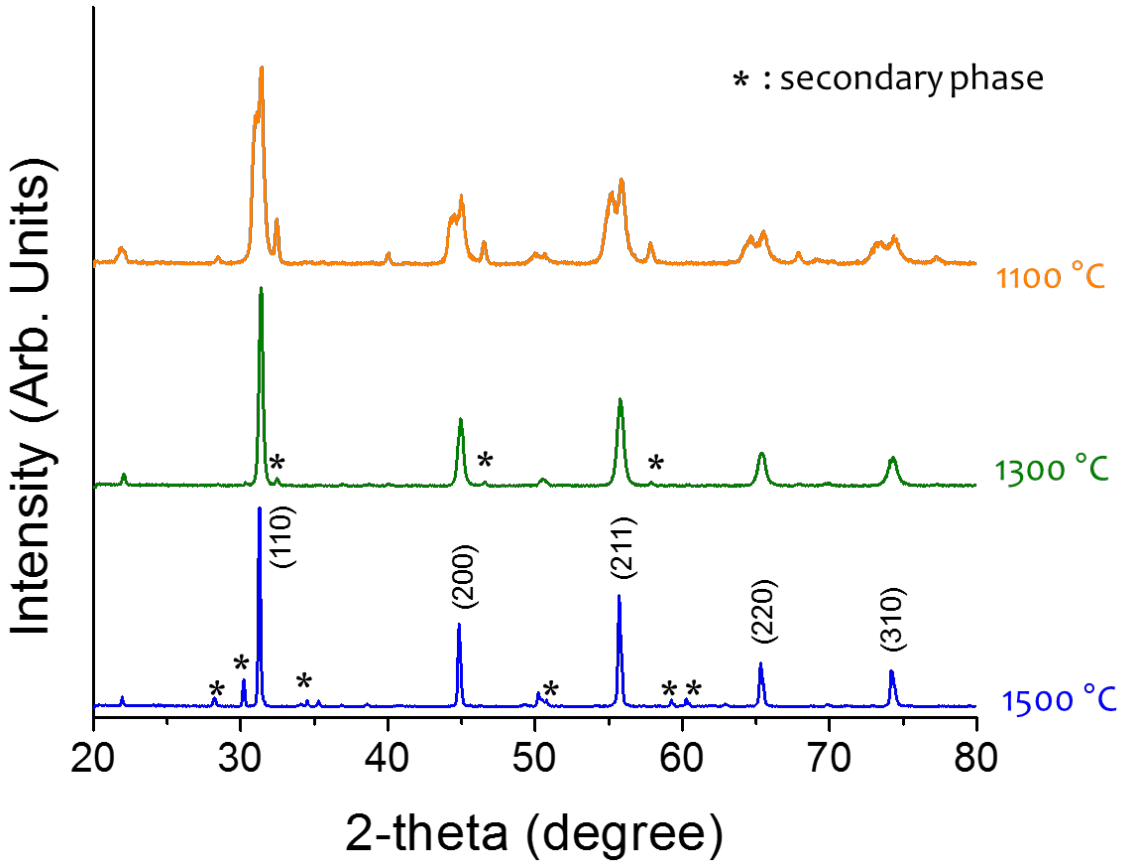

Figure 3.1 XRD patterns of composition #S0, $Sr(Zr_{0.25}Sn_{0.25}Ti_{0.25}Hf_{0.25})O_3$.

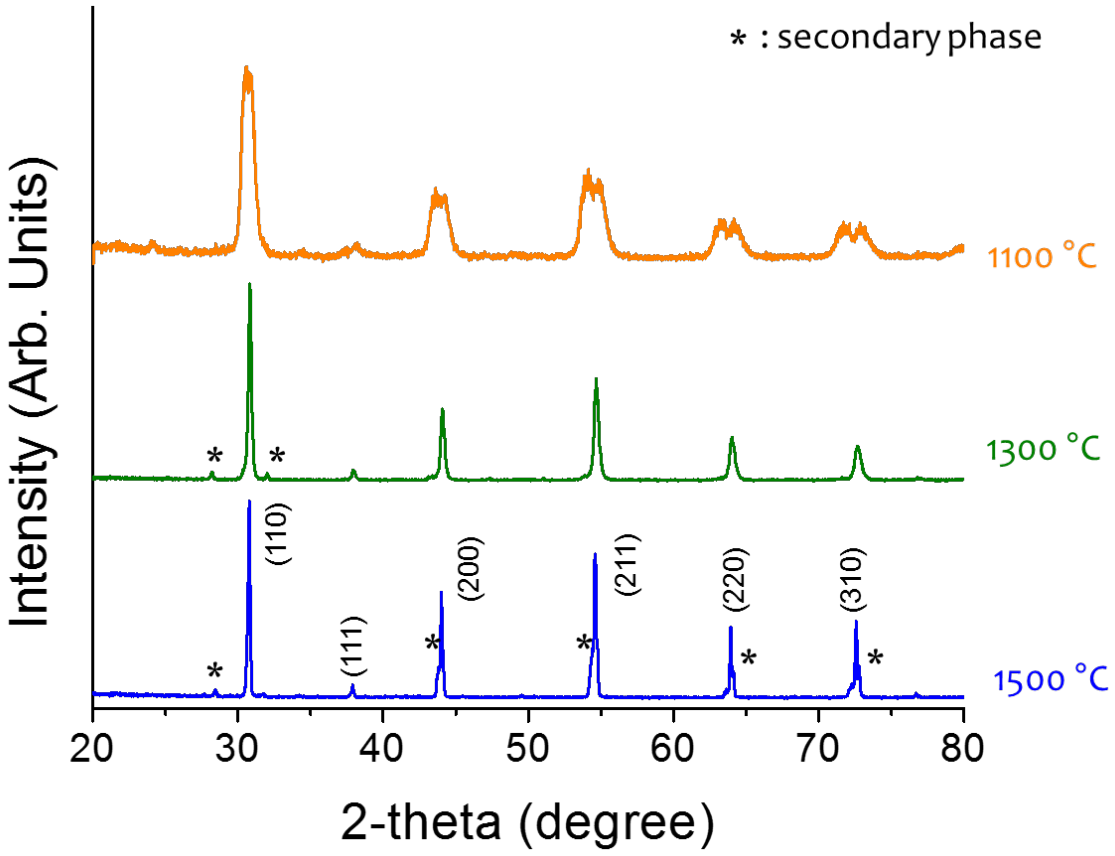

Figure 3.2 XRD patterns of composition #B0, $Ba(Zr_{0.25}Sn_{0.25}Ti_{0.25}Hf_{0.25})O_3$.

Table 1. Tolerance factor (t), lattice parameter (a), cohesive energy (E_c) and transition sequences of the simple 2:4 perovskites in this study. The bold Roman numeral or 'tricrit.' label refers to the order of the transition (first order, second order or tricritical). Question marks indicate uncertainty.

	$BaCeO_3$	$SrZrO_3$	$SrHfO_3$	$PbZrO_3$	$CaTiO_3$	$PbHfO_3$	$PbSnO_3$	$BaPbO_3$	$SrRuO_3$	$SrTiO_3$	$BaZrO_3$	$BaHfO_3$	$PbTiO_3$	$BaTiO_3$
t	0.9428	0.9531	0.9577	0.9701	0.9730	0.9748	0.9844	0.9850	1.0014	1.0091	1.0111	1.0160	1.0272	1.0706
a (Å)	4.44	4.15	4.11	4.16	3.89	4.15	4.07	4.29	3.97	3.91	4.20	4.17	3.97	4.02
E_c (eV)	−36.35	−40.09	−37.63	−37.37	−38.75	−35.47	−29.80	−27.92	−34.05	−38.73	−40.57	−38.42	−36.13	−38.78
Ref.	[42]	[43]	[44]	[34, 40]	[45]	[32, 33]	[36]	[46]	[47]	[48]	[49]	[50]	[6]	[6]
						Transition sequence								
	$Pm\bar{3}m$	$Pm\bar{3}m$	$Pm\bar{3}m$	$Pm\bar{3}m$	$Pm\bar{3}m$	$Pm\bar{3}m$	$Pm\bar{3}m$	$Pm\bar{3}m$	$Pm\bar{3}m$	$Pm\bar{3}m$	$Pm\bar{3}m$	$Pm\bar{3}m$	$Pm\bar{3}m$	$Pm\bar{3}m$
	$(a^0a^0a^0)$	$(a^0a^0a^0)$	$(a^0a^0a^0)$	$(a^0a^0a^0)$	$(a^0a^0a^0)$	$(a^0a^0a^0)$	$(a^0a^0a^0)$	$(a^0a^0a^0)$	$(a^0a^0a^0)$	$(a^0a^0a^0)$	$(a^0a^0a^0)$	$(a^0a^0a^0)$	$(a^0a^0a^0)$	$(a^0a^0a^0)$
	1200 K	1380 K	1380 K	~520 K	1634 K	~484 K	~400 K	723 K	950 K	105 K			763 K	393 K
	↔	↔	↔	↔	↔	↔	↔	↔	↔	↔			↔	↔
	II	**tricrit.**	**II**	?	**tricrit.**	?	?	**tricrit.**	**II** (?)	**II**			**I**	**I**
	$R\bar{3}c$	$I4/mcm$	$I4/mcm$	?	$I4/mcm$	Tetrag. (?)	Mono. (?)	$I4/mcm$	$I4/mcm$	$I4/mcm$			$P4mm$	$P4mm$
	$(a^-a^-a^-)$	$(a^0a^0c^-)$	$(a^0a^0c^-)$		$(a^0a^0c^-)$			$(a^0a^0c^-)$	$(a^0a^0c^-)$	$(a^0a^0c^-)$			$(a^0a^0a^0)$	$(a^0a^0a^0)$
	673 K	1113 K	1113 K	?	1500 K	435 K		548 K	825 K					273 K
	↔	↔	↔	↔	↔	↔		↔	↔					↔
	I	**I**	**II**	?	**I**	?		**I**	**I**					**I**
	$Imma$	$Imma$	$Cmcm$	$Pbam$	$Cmcm$	$Pbam$		$Imma$	$Imma$					$Amm2$
	$(a^0b^-b^-)$	$(a^0b^-b^-)$	$(a^0b^+c^-)$	$(a^0b^-b^-)$	$(a^0b^+c^-)$	$(a^0b^-b^-)$		$(a^0b^-b^-)$	$(a^0b^-b^-)$					$(a^0a^0a^0)$
	573 K	1023 K	1023 K		1380 K			?	685 K					183 K
	↔	↔	↔		↔			↔	↔					↔
	II	**II**	**I**		**I**			**II** (?)	**II** (?)					**I**
	$Pnma$	$Pnma$	$Pnma$		$Pnma$			$Pnma$ (?)	$Pnma$					$R3m$
	$(a^+b^-b^-)$	$(a^+b^-b^-)$	$(a^+b^-b^-)$		$(a^+b^-b^-)$			$(a^+b^-b^-)$	$(a^+b^-b^-)$					$(a^0a^0a^0)$

Figure 3.3 Transition sequence of several common ABO_3 perovskites [27].

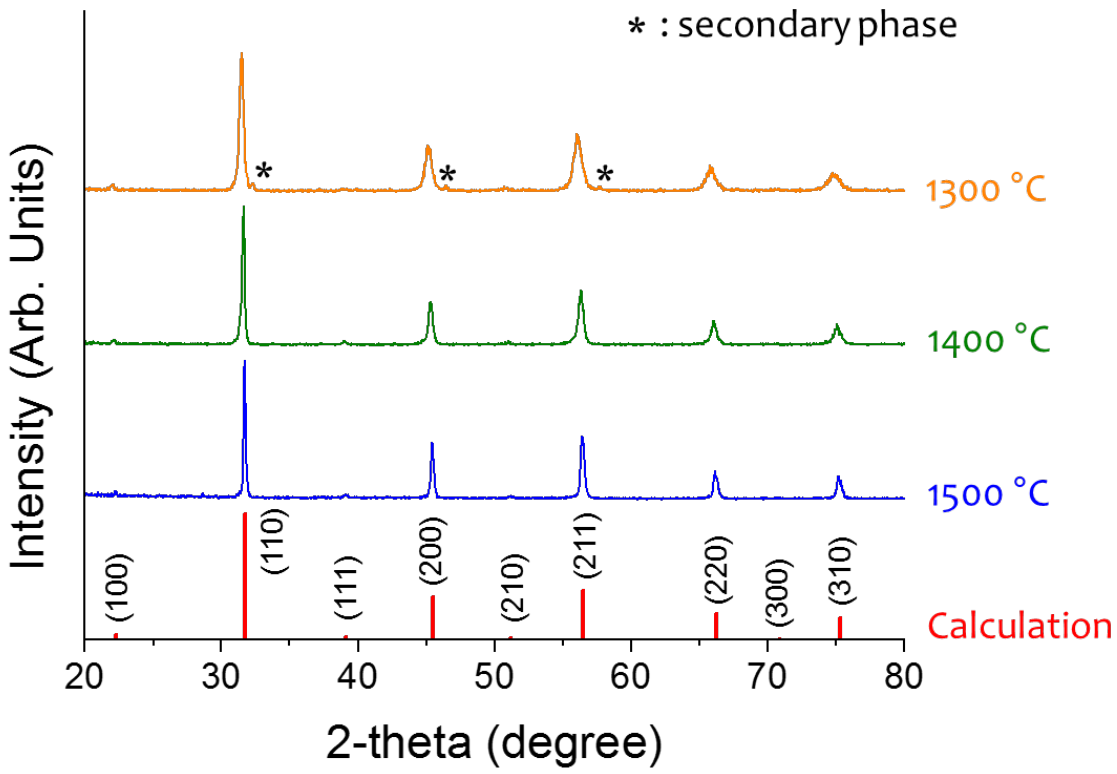

Figure 3.4 XRD pattern of composition #S1, $Sr(Zr_{0.2}Sn_{0.2}Ti_{0.2}Hf_{0.2}Mn_{0.2})O_3$.

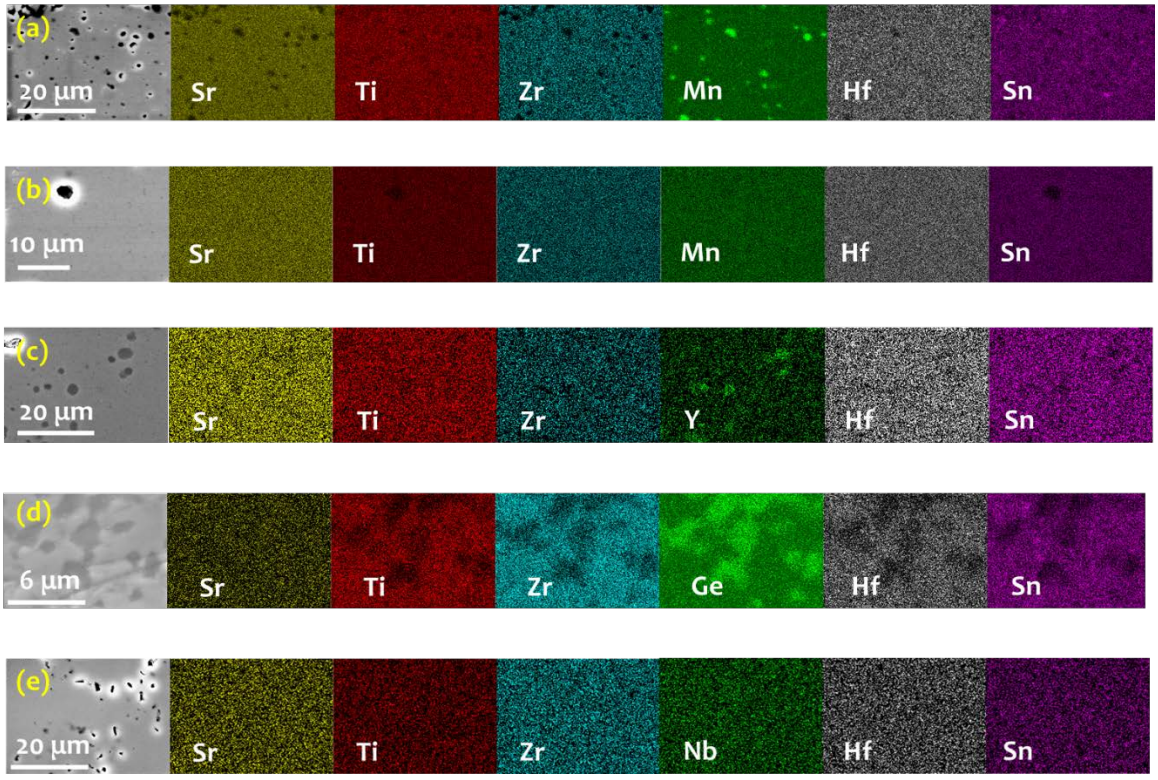

Figure 3.5 (a) EDS mapping of composition #S1, $Sr(Zr_{0.2}Sn_{0.2}Ti_{0.2}Hf_{0.2}Mn_{0.2})O_3$ @1400 °C ; (b) EDS mapping of composition #S1, $Sr(Zr_{0.2}Sn_{0.2}Ti_{0.2}Hf_{0.2}Mn_{0.2})O_3$ @1500 °C ; (c) EDS mapping of composition #S3, $Sr(Zr_{0.2}Sn_{0.2}Ti_{0.2}Hf_{0.2}Y_{0.2})O_{3-x}$ @1500 °C ; (d) EDS mapping of composition #S4, $Sr(Zr_{0.2}Sn_{0.2}Ti_{0.2}Hf_{0.2}Ge_{0.2})O_3$ @1300 °C ; (e) EDS mapping of composition #S1, $Sr(Zr_{0.2}Sn_{0.2}Ti_{0.2}Hf_{0.2}Nb_{0.2})O_3$ @1500 °C.

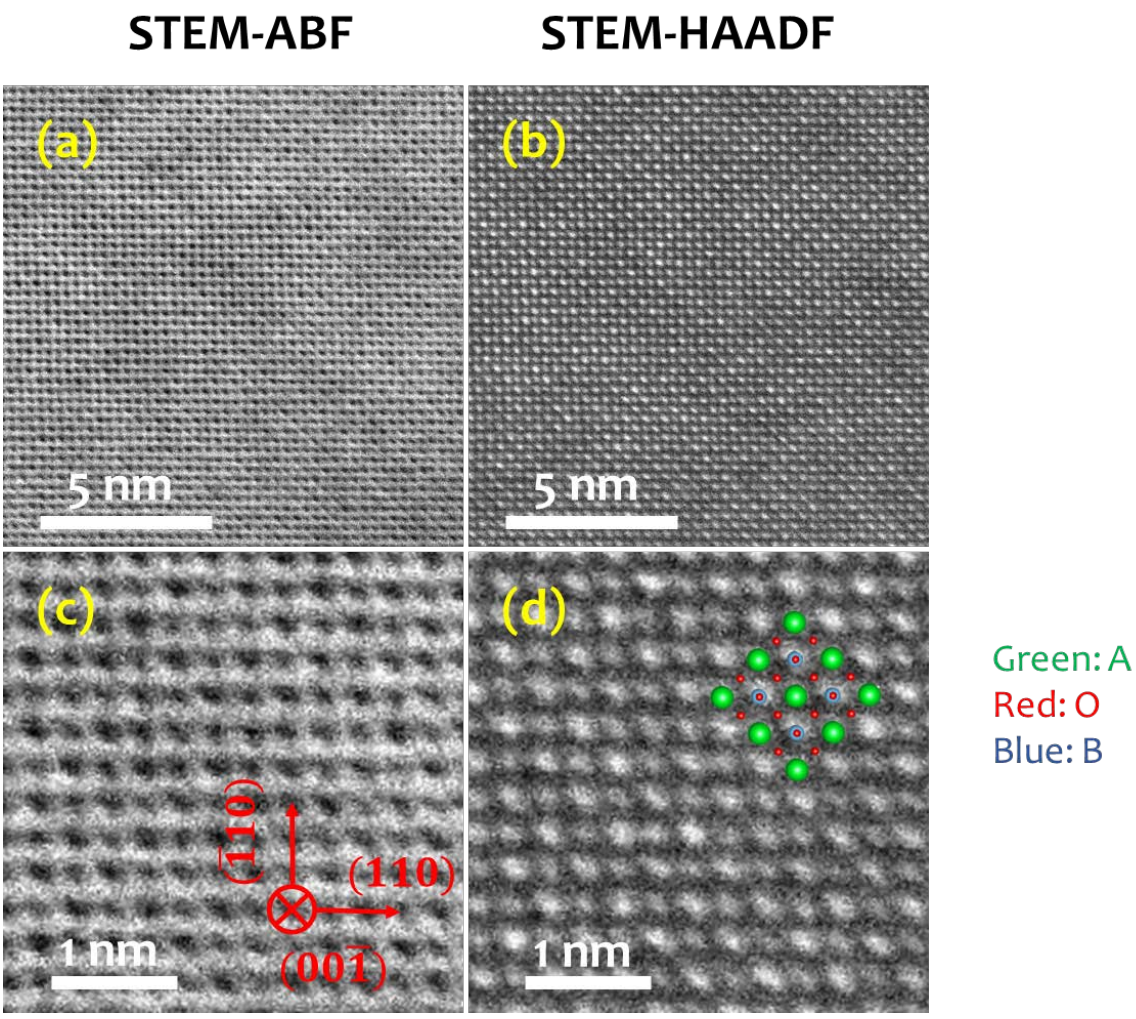

Figure 3.6 STEM ABF and HAADF images of composition #S1, $Sr(Zr_{0.2}Sn_{0.2}Ti_{0.2}Hf_{0.2}Mn_{0.2})O_3$.

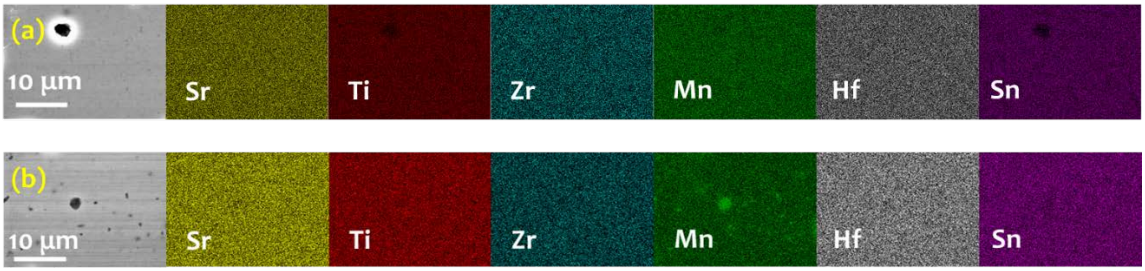

Figure 3.7 (a) EDS mapping of composition #S1, $Sr(Zr_{0.2}Sn_{0.2}Ti_{0.2}Hf_{0.2}Mn_{0.2})O_3$, sintered at 1500 °C for 2 hours and then air quenched; (b) EDS mapping of composition #S1, $Sr(Zr_{0.2}Sn_{0.2}Ti_{0.2}Hf_{0.2}Mn_{0.2})O_3$, sintered at 1500 °C for 2 hours then held at 1400 °C for 2 hours and then air quenched.

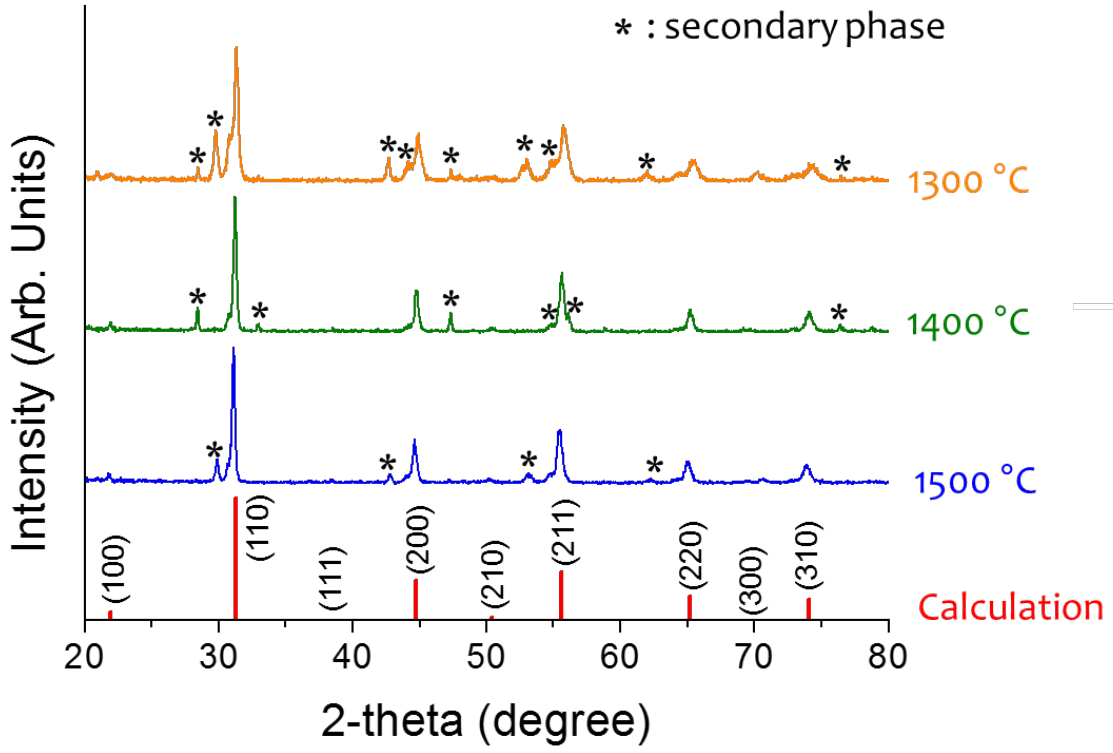

Figure 3.8 XRD pattern of composition #S2, $Sr(Zr_{0.2}Sn_{0.2}Ti_{0.2}Hf_{0.2}Ce_{0.2})O_3$.

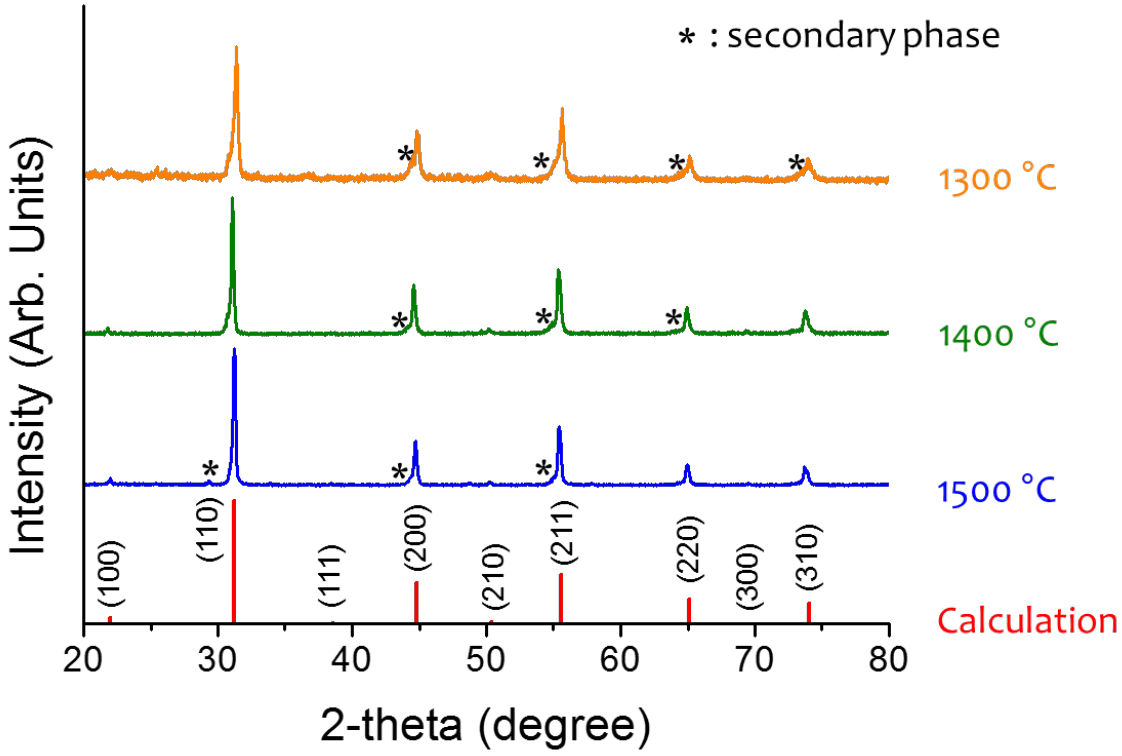

Figure 3.9 XRD pattern of composition #S3, $Sr(Zr_{0.2}Sn_{0.2}Ti_{0.2}Hf_{0.2}Y_{0.2})O_{3-x}$.

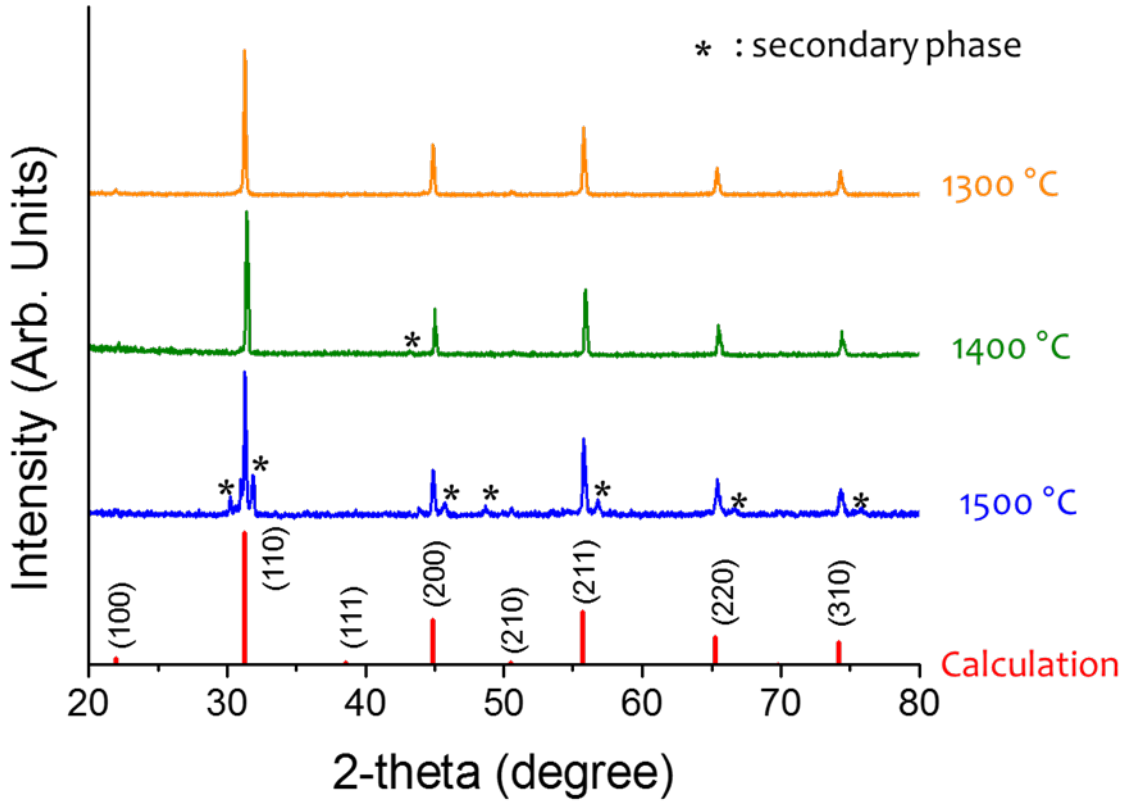

Figure 3.10 XRD pattern of composition #S4, $Sr(Zr_{0.2}Sn_{0.2}Ti_{0.2}Hf_{0.2}Ge_{0.2})O_3$.

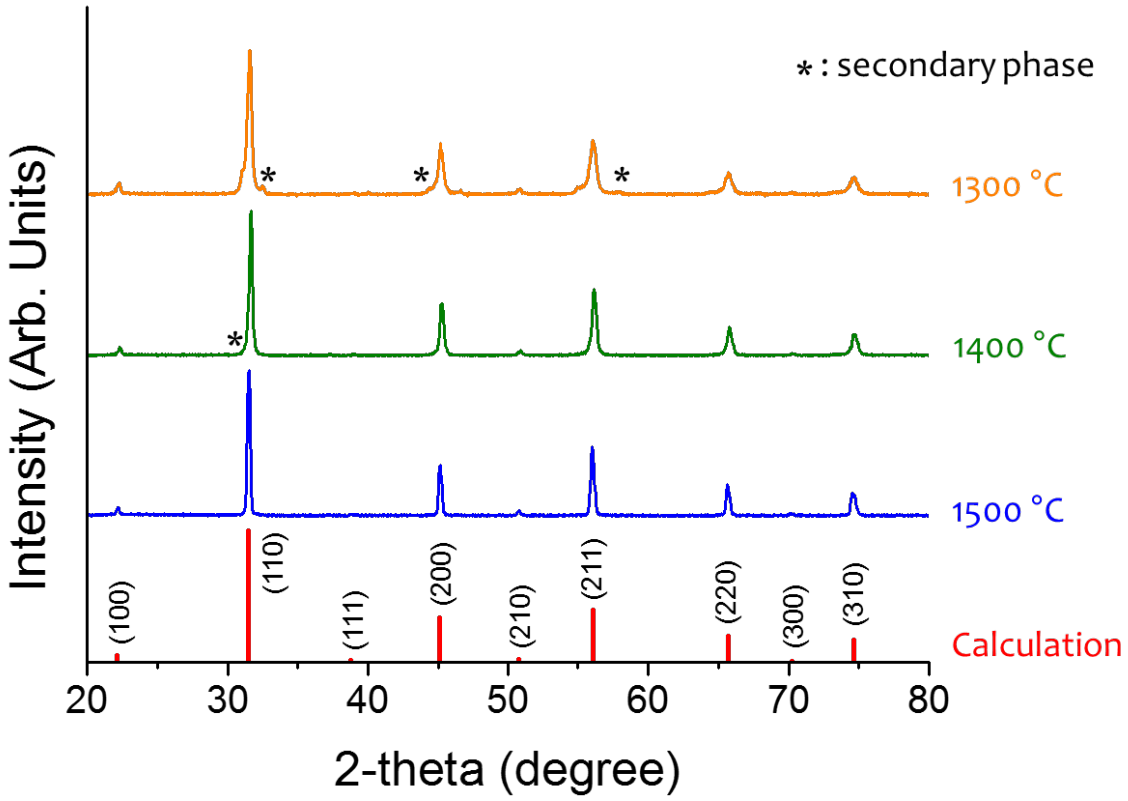

Figure 3.11 XRD pattern of composition #S5, $Sr(Zr_{0.2}Sn_{0.2}Ti_{0.2}Hf_{0.2}Nb_{0.2})O_3$.

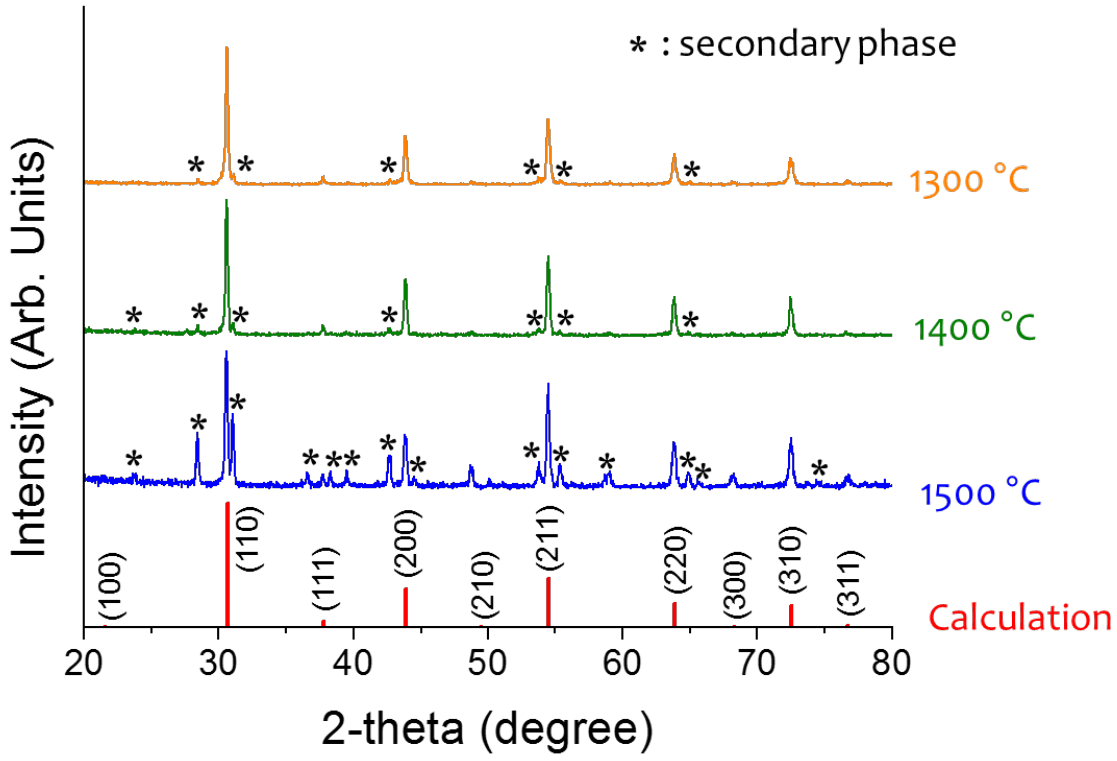

Figure 3.12 XRD pattern of composition #B1, $Ba(Zr_{0.2}Sn_{0.2}Ti_{0.2}Hf_{0.2}Mn_{0.2})O_3$.

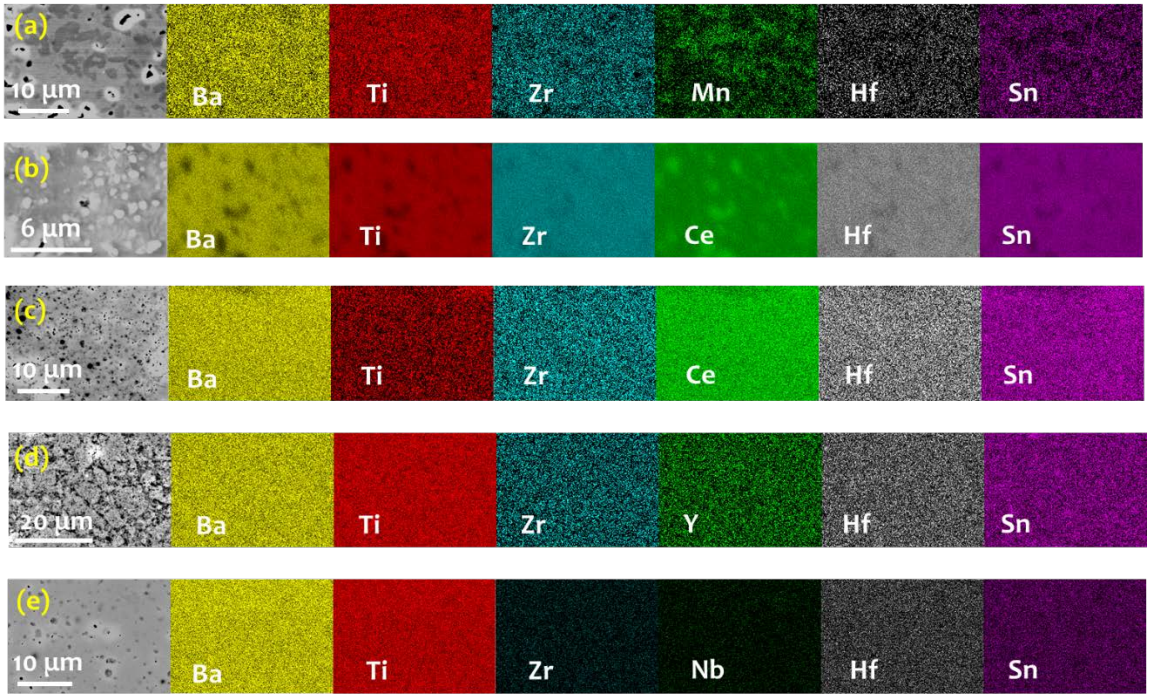

Figure 3.13 (a) EDS mapping of composition #B1, $Ba(Zr_{0.2}Sn_{0.2}Ti_{0.2}Hf_{0.2}Mn_{0.2})O_3$ @1500 °C ; (b) EDS mapping of composition #B2, $Ba(Zr_{0.2}Sn_{0.2}Ti_{0.2}Hf_{0.2}Ce_{0.2})O_3$ @1500 °C ; (c) EDS mapping of composition #B2, $Ba(Zr_{0.2}Sn_{0.2}Ti_{0.2}Hf_{0.2}Ce_{0.2})O_3$ @1300 °C ; (d) EDS mapping of composition #B3, $Ba(Zr_{0.2}Sn_{0.2}Ti_{0.2}Hf_{0.2}Y_{0.2})O_{3-x}$ @1300 °C ; (e) EDS mapping of composition #B5, $Ba(Zr_{0.2}Sn_{0.2}Ti_{0.2}Hf_{0.2}Nb_{0.2})O_3$ @1300 °C.

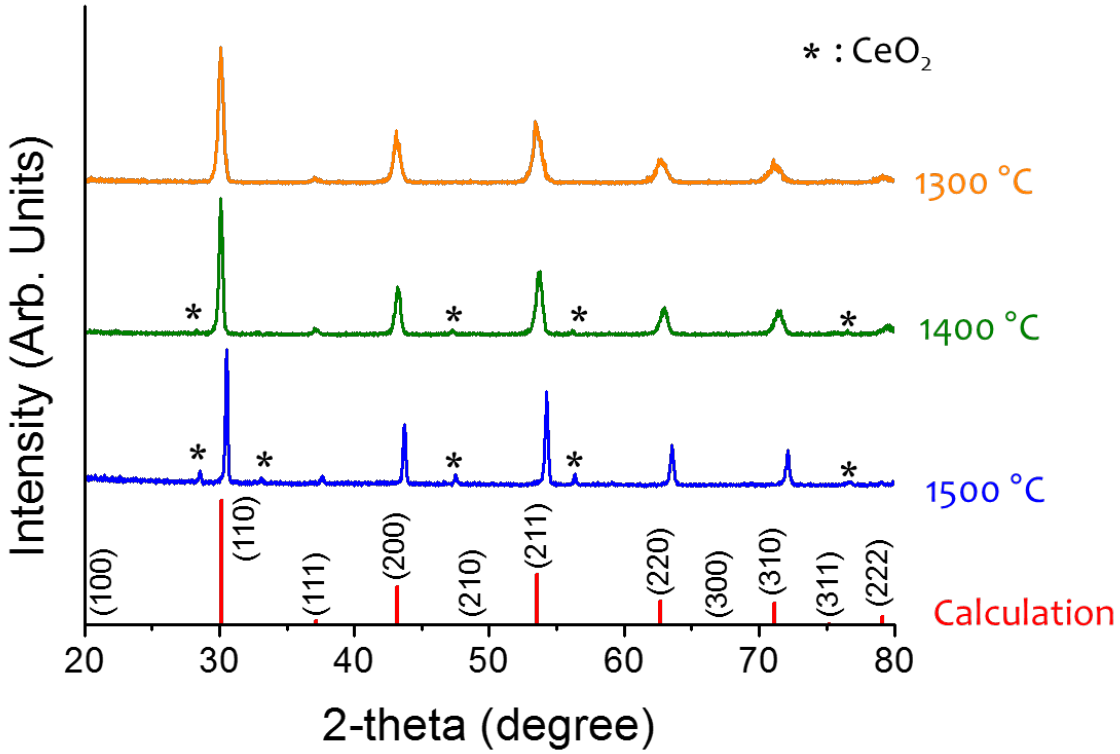

Figure 3.14 XRD pattern of composition #B2, $Ba(Zr_{0.2}Sn_{0.2}Ti_{0.2}Hf_{0.2}Ce_{0.2})O_3$.

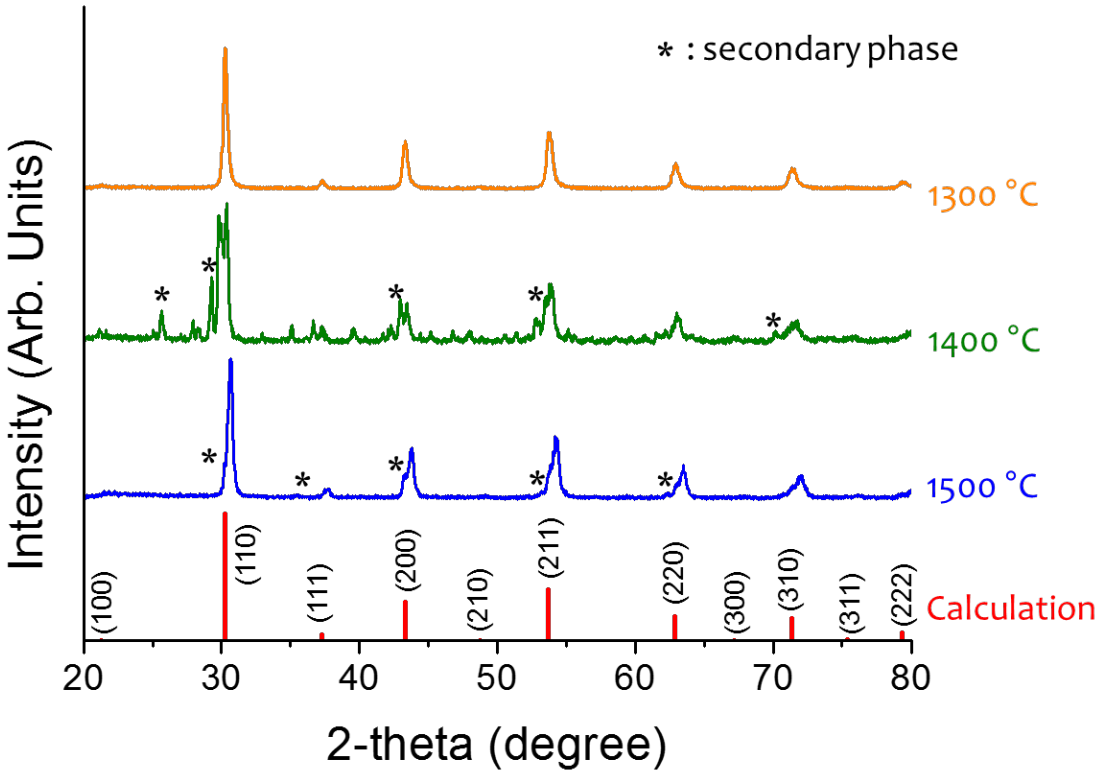

Figure 3.15 XRD pattern of composition #B3, $Ba(Zr_{0.2}Sn_{0.2}Ti_{0.2}Hf_{0.2}Y_{0.2})O_{3-x}$.

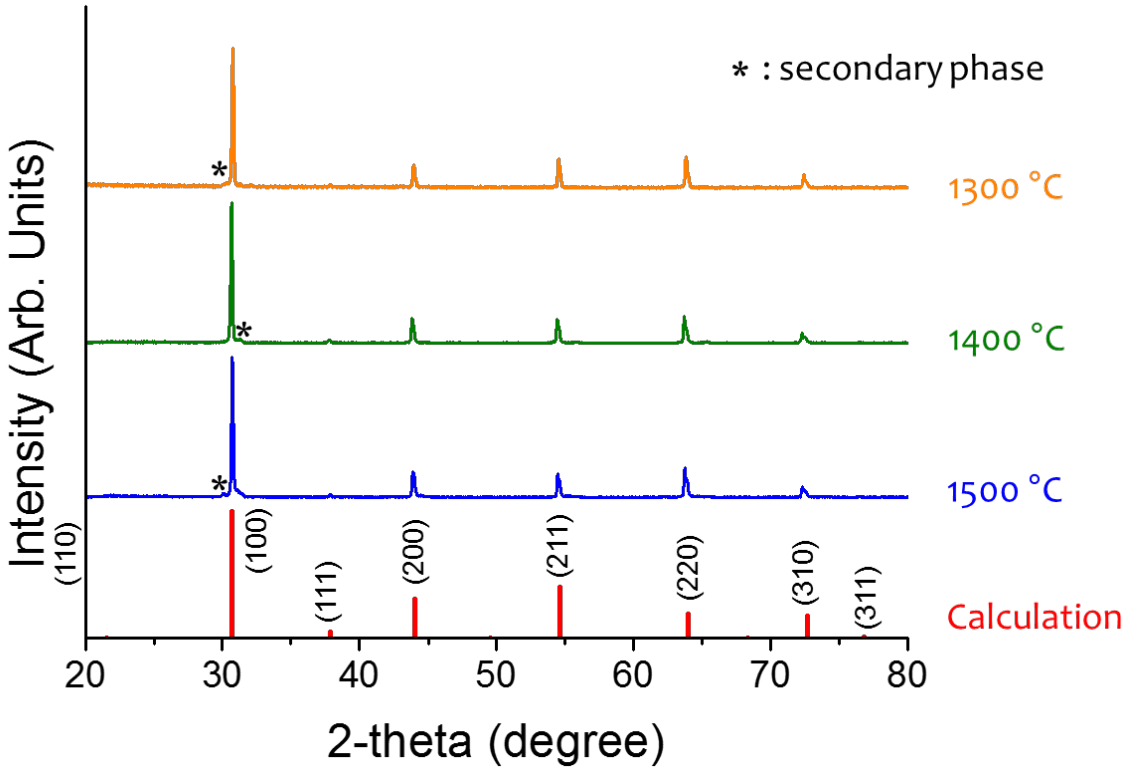

Figure 3.16 XRD pattern of composition #B4, $Ba(Zr_{0.2}Sn_{0.2}Ti_{0.2}Hf_{0.2}Ge_{0.2})O_3$.

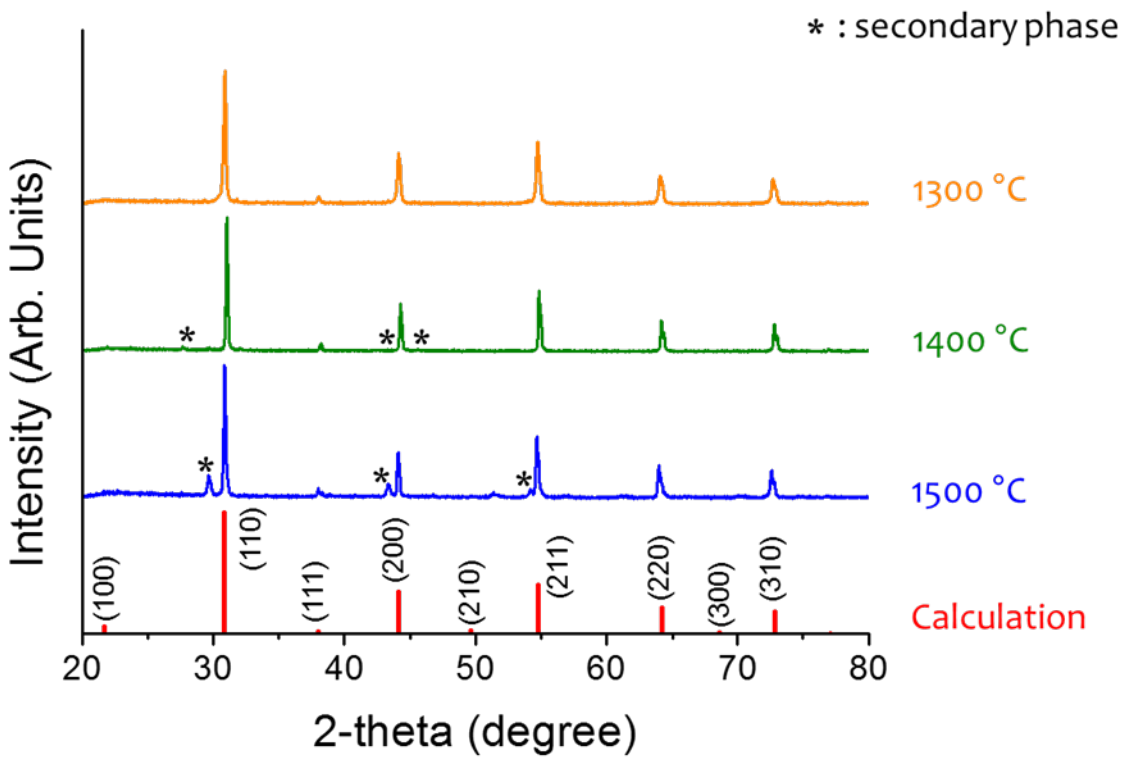

Figure 3.17 XRD pattern of composition #B5, $Ba(Zr_{0.2}Sn_{0.2}Ti_{0.2}Hf_{0.2}Nb_{0.2})O_3$.

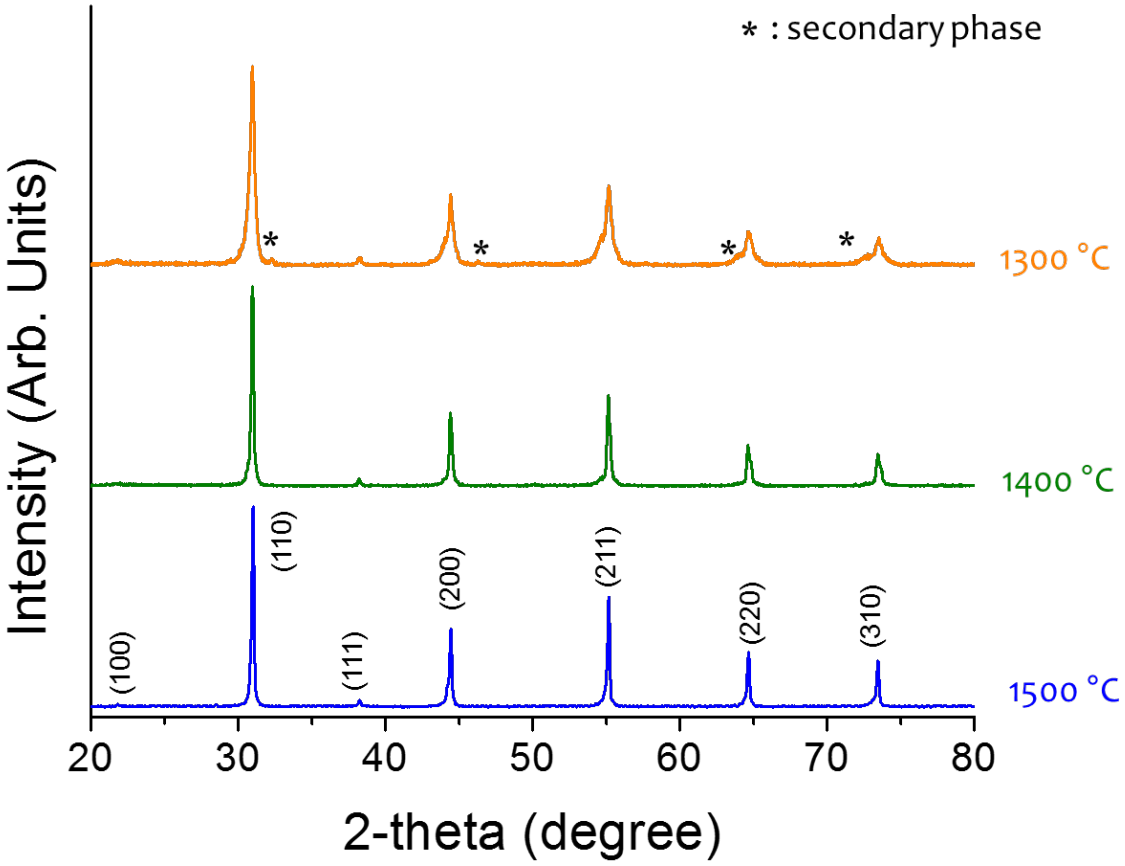

Figure 3.18 XRD pattern of composition #BS1, $(Ba_{0.5}Sr_{0.5})(Zr_{0.2}Sn_{0.2}Ti_{0.2}Hf_{0.2}Nb_{0.2})O_3$.

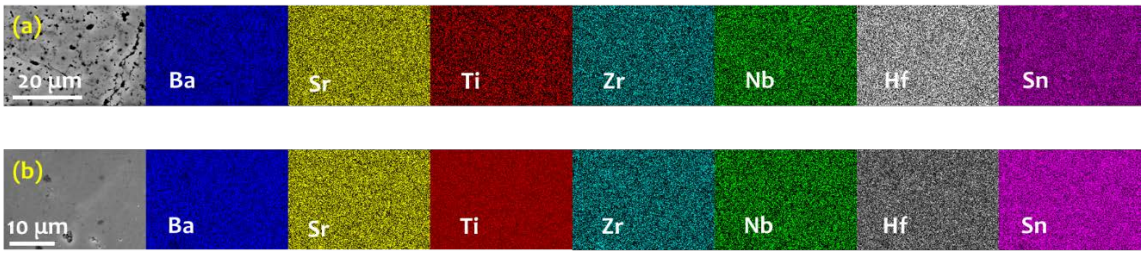

Figure 3.19 (a) EDS mapping of composition #BS1, $(Ba_{0.5}Sr_{0.5})(Zr_{0.2}Sn_{0.2}Ti_{0.2}Hf_{0.2}Nb_{0.2})O_3$ @1400 °C ; (b) EDS mapping of composition #BS1, $(Ba_{0.5}Sr_{0.5})(Zr_{0.2}Sn_{0.2}Ti_{0.2}Hf_{0.2}Nb_{0.2})O_3$ @1500 °C.

Table 2.1 Summary of original chemicals.

	Components	Original Chemicals (with stoichiometric mole fraction)					
#S0	$Sr(Zr_{0.2}Sn_{0.2}Ti_{0.2}Hf_{0.2})O_3$	N/A	SnO_2	$BaTiO_3$	$BaZrO_3$	BaO	HfO_2
#S1	$Sr(Zr_{0.2}Sn_{0.2}Ti_{0.2}Hf_{0.2}Mn_{0.2})O_3$	MnO_2					
#S2	$Sr(Zr_{0.2}Sn_{0.2}Ti_{0.2}Hf_{0.2}Ce_{0.2})O_3$	CeO_2					
#S3	$Sr(Zr_{0.2}Sn_{0.2}Ti_{0.2}Hf_{0.2}Y_{0.2})O_{3-x}$	Y_2O_3					
#S4	$Sr(Zr_{0.2}Sn_{0.2}Ti_{0.2}Hf_{0.2}Ge_{0.2})O_3$	GeO_2					
#S5	$Sr(Zr_{0.2}Sn_{0.2}Ti_{0.2}Hf_{0.2}Nb_{0.2})O_3$	NbO_2					
#B0	$Ba(Zr_{0.2}Sn_{0.2}Ti_{0.2}Hf_{0.2})O_3$	N/A	$SrSnO_3$	$SrTiO_3$	$SrZrO_3$	SrO	
#B1	$Ba(Zr_{0.2}Sn_{0.2}Ti_{0.2}Hf_{0.2}Mn_{0.2})O_3$	MnO_2					
#B2	$Ba(Zr_{0.2}Sn_{0.2}Ti_{0.2}Hf_{0.2}Ce_{0.2})O_3$	CeO_2					
#B3	$Ba(Zr_{0.2}Sn_{0.2}Ti_{0.2}Hf_{0.2}Y_{0.2})O_{3-x}$	Y_2O_3					
#B4	$Ba(Zr_{0.2}Sn_{0.2}Ti_{0.2}Hf_{0.2}Ge_{0.2})O_3$	GeO_2					
#B5	$Ba(Zr_{0.2}Sn_{0.2}Ti_{0.2}Hf_{0.2}Nb_{0.2})O_3$	NbO_2					

Table 3.1 Intensity of elements in composition #S1 in STEM images, Z is the atomic number of elements.

	Ti	Zr	Sn	Hf	Mn	Sr
Z	22	40	50	72	25	38
$Z^{1.7}$	191	529	773	1437	238	485

Table 3.2 Summary of all compositions: Ion radius: R[Sr^{2+}]: 1.440 Å, R[Ba^{2+}]: 1.610 Å, R[O^{2-}]: 1.350 Å, tolerance factor (t) = $\frac{R_A+R_O}{\sqrt{2}(R_B+R_O)}$; Yes: single phase, 1: secondary phase cannot be discovered from XRD, 2: small amount of secondary phase (XRD intensity of secondary phase is less than 6%) , 3: large amount of secondary phase (XRD intensity of secondary phase is more than 6%).

	Components	Single phase?			Average R_B/Å	Standard deviation R_B	$\delta(R_B)$	tolerance factor t
		1300 ℃	1400 ℃	1500 ℃				
#S1	$Sr(Zr_{0.2}Sn_{0.2}Ti_{0.2}Hf_{0.2}Mn_{0.2})O_3$	2	1	Yes	0.651	0.07	8.7%	0.99
#S2	$Sr(Zr_{0.2}Sn_{0.2}Ti_{0.2}Hf_{0.2}Ce_{0.2})O_3$	3	3	3	0.719	0.09	10.5%	0.95
#S3	$Sr(Zr_{0.2}Sn_{0.2}Ti_{0.2}Hf_{0.2}Y_{0.2})O_{3-x}$	3	2	1	0.725	0.10	11.9%	0.95
#S4	$Sr(Zr_{0.2}Sn_{0.2}Ti_{0.2}Hf_{0.2}Ge_{0.2})O_3$	1	1	3	0.651	0.07	8.7%	0.99
#S5	$Sr(Zr_{0.2}Sn_{0.2}Ti_{0.2}Hf_{0.2}Nb_{0.2})O_3$	2	1	Yes	0.681	0.04	4.8%	0.97
#B1	$Ba(Zr_{0.2}Sn_{0.2}Ti_{0.2}Hf_{0.2}Mn_{0.2})O_3$	3	3	3	0.651	0.07	8.7%	1.05
#B2	$Ba(Zr_{0.2}Sn_{0.2}Ti_{0.2}Hf_{0.2}Ce_{0.2})O_3$	Yes	2	3	0.719	0.09	10.5%	1.01
#B3	$Ba(Zr_{0.2}Sn_{0.2}Ti_{0.2}Hf_{0.2}Y_{0.2})O_{3-x}$	Yes	3	3	0.725	0.10	11.9%	1.01
#B4	$Ba(Zr_{0.2}Sn_{0.2}Ti_{0.2}Hf_{0.2}Ge_{0.2})O_3$	2	2	3	0.651	0.07	8.7%	1.05
#B5	$Ba(Zr_{0.2}Sn_{0.2}Ti_{0.2}Hf_{0.2}Nb_{0.2})O_3$	Yes	2	3	0.681	0.04	4.8%	1.03
#BS1	$(Ba_{0.5}Sr_{0.5})(Zr_{0.2}Sn_{0.2}Ti_{0.2}Hf_{0.2}Nb_{0.2})O_3$	1	Yes	Yes	0.681	0.04	8.7%	1.00

Table 3.3 Summary of lattice constant of compositions that can form a homogeneous single phase.

	Components	Lattice constant a/Å	Empirical calculation a/Å	Error	Standard deviation
#S1	$Sr(Zr_{0.2}Sn_{0.2}Ti_{0.2}Hf_{0.2}Mn_{0.2})O_3$	3.992	4.032	1.0%	0.07
#S5	$Sr(Zr_{0.2}Sn_{0.2}Ti_{0.2}Hf_{0.2}Nb_{0.2})O_3$	4.021	4.067	1.1%	0.04
#B2	$Ba(Zr_{0.2}Sn_{0.2}Ti_{0.2}Hf_{0.2}Ce_{0.2})O_3$	4.192	4.198	0.2%	0.09
#B3	$Ba(Zr_{0.2}Sn_{0.2}Ti_{0.2}Hf_{0.2}Y_{0.2})O_{3-x}$	4.179	4.205	0.6%	0.10
#B5	$Ba(Zr_{0.2}Sn_{0.2}Ti_{0.2}Hf_{0.2}Nb_{0.2})O_3$	4.105	4.155	1.2%	0.04
#BS1	$(Ba_{0.5}Sr_{0.5})(Zr_{0.2}Sn_{0.2}Ti_{0.2}Hf_{0.2}Nb_{0.2})O_3$	4.072	4.111	1.0%	0.06

References

[1] R.S. Roth, Journal of Research of the National Bureau of Standards 58 (1957) 14.

[2] V.M. Goldschmidt, Naturwissenschaften, 14 (1926) 477-485.

[3] N. Ramadass, Materials Science and Engineering, 36 (1978) 231-239.

[4] C. Li, X. Lu, W. Ding, L. Feng, Y. Gao, Z. Guo, Acta Crystallographica Section B: Structural Science, 64 (2008) 702-707.

[5] N.Q. Minh, Journal of the American Ceramic Society, 76 (1993) 563-588.

[6] A. Jun, J. Kim, J. Shin, G. Kim, ChemElectroChem, 3 (2016) 511-530.

[7] J. Shi, L. Guo, Progress in Natural Science: Materials International, 22 (2012) 592-615.

[8] F.E. Osterloh, Chemistry of Materials, 20 (2008) 35-54.

[9] M.A. Peña, J.L.G. Fierro, Chemical Reviews, 101 (2001) 1981-2018.

[10] M.S. Wrighton, A.B. Ellis, P.T. Wolczanski, D.L. Morse, H.B. Abrahamson, D.S. Ginley, Journal of the American Chemical Society, 98 (1976) 2774-2779.

[11] G. Zhang, G. Liu, L. Wang, J.T.S. Irvine, Chemical Society Reviews, 45 (2016) 5951-5984.

[12] N. Wang, M. Cao, Z. He, C. Diao, Q. Zhang, Y. Zhang, J. Dai, F. Zeng, H. Hao, Z. Yao, H. Liu, Ceram. Int., 42 (2016) 13593-13600.

[13] Z. Wang, M. Cao, Q. Zhang, H. Hao, Z. Yao, Z. Wang, Z. Song, Y. Zhang, W. Hu, H. Liu, Journal of the American Ceramic Society, 98 (2015) 476-482.

[14] J. Karczewski, B. Riegel, M. Gazda, P. Jasinski, B. Kusz, Journal of Electroceramics, 24 (2010) 326-330.

[15] Y. Zhang, T. Zuo, Z. Tang, M.C. Gao, K.A. Dahmen, P.K. Liaw, Z. Lu, Progress in Materials Science, 61 (2014) 1-93.

[16] Y. JW, Ann Chim Sci Mater, 31 (2006) 633.

[17] M.A. Hemphill, T. Yuan, G.Y. Wang, J.W. Yeh, C.W. Tsai, A. Chuang, P.K. Liaw, Acta Materialia, 60 (2012) 5723-5734.

[18] C.J. Tong, M.R. Chen, S.K. Chen, J.W. Yeh, T.T. Shun, S.J. Lin, S.Y. Chang, Metallurgical And Materials Transactions a-Physical Metallurgy And Materials Science, 36A (2005) 1263-1271.

[19] M.H. Chuang, M.H. Tsai, W.R. Wang, S.J. Lin, J.W. Yeh, Acta Materialia, 59 (2011) 6308-6317.

[20] C.A. Gearhart, American Journal of Physics, 58 (1990) 468-480.

[21] C.M. Rost, E. Sachet, T. Borman, A. Moballegh, E.C. Dickey, D. Hou, J.L. Jones, S. Curtarolo, J.-P. Maria, Nat Commun, 6 (2015).

[22] D. Bérardan, S. Franger, D. Dragoe, A. Meena, N. Dragoe, physica status solidi (RRL) - Rapid Research Letters, 10 (2016) 328-333.

[23] J. Gild, Y. Zhang, T. Harrington, S. Jiang, T. Hu, M.C. Quinn, W.M. Mellor, N. Zhou, K. Vecchio, J. Luo, Scientific Reports, 6 (2016) 37946.

[24] K. Ishizuka, Ultramicroscopy, 90 (2002) 71-83.

[25] A.S. Verma, V.K. Jindal, Journal of Alloys and Compounds, 485 (2009) 514-518.

[26] R.L. Moreira, A. Dias, Journal of Physics and Chemistry of Solids, 68 (2007) 1617-1622.

[27] G. Pavel, J.B. Andrew, Journal of Physics: Condensed Matter, 19 (2007) 176201.